Petroleum Science 23 (2026) 3539–3555

Contents lists available at ScienceDirect

Petroleum Science

journal homepage: www.keaipublishing.com/en/journals/petroleum-science

Original Paper

Mechanisms of CO_2 nanobubble-enhanced oil recovery: Interfacial regulation and flow behavior control in porous media

Xu-Wen Qin [a,b], Bei Wei [a,b], Yong-Sheng Liu [a,b], Qian Chen [a,b], Hao-Yu Zheng [a,b], Er-Meng Zhao [d], Qing-Jun Du [a,b], Kang Zhou [e], Yong-Ge Liu [a,b], Wei-Bing Tian [a,b], Jian Hou [a,b,c,*]

[a] State Key Laboratory of Deep Oil and Gas, China University of Petroleum (East China), Qingdao, 266580, Shandong, China
[b] School of Petroleum Engineering, China University of Petroleum (East China), Qingdao, 266580, Shandong, China
[c] Laboratory for Marine Mineral Resources, Qingdao National Laboratory for Marine Science and Technology, Qingdao, 266237, Shandong, China
[d] School of Energy Resource, China University of Geosciences (Beijing), Beijing, 100083, China
[e] College of Energy and Mining Engineering, Shandong University of Science and Technology, Qingdao, 266590, Shandong, China

ARTICLE INFO

Article history:
Received 10 November 2025
Received in revised form
5 March 2026
Accepted 8 March 2026
Available online 12 March 2026

Edited by Yan-Hua Sun

Keywords:
Nanobubbles
Enhanced oil recovery
Interfacial properties
Flow characteristics through porous media
Oil displacement mechanisms

ABSTRACT

Nanobubbles (NBs) have unique physicochemical properties, including a large specific surface area and high mass transfer efficiency. They can be produced using environmentally friendly, low-cost physical methods, making them a promising green agent for enhanced oil recovery (EOR). However, the mechanism by which NBs enhance oil recovery remains unclear. In this study, we systematically investigate the stability of NBs under varying conditions (e.g., salinity and temperature) using nanoparticle tracking analysis. The interfacial properties of NBs were evaluated through interfacial tension measurements, contact angle analysis, and oil film detachment experiments. Furthermore, multiscale flow experiments in porous media and oil displacement experiments were conducted to reveal the flow characteristics and oil displacement mechanisms of NBs. Results demonstrate that NBs exhibit excellent thermal stability, salt tolerance, shear resistance, and temporal stability. They can reduce oil–water interfacial tension while enhancing the solid interface's affinity for the aqueous phase and its oil-repellent properties. NBs improve oil recovery through multiple synergistic mechanisms (6%–9%) over conventional water flooding. NBs facilitate the penetration of the displacing fluid into microporous regions that are typically inaccessible to conventional water flooding. Simultaneously, Ostwald ripening—where smaller bubbles dissolve and larger ones grow via gas diffusion—in porous media leads to pore-throat blockage, increasing flow resistance and improving sweep efficiency. These synergistic mechanisms enhance the sweep efficiency of the displacing fluid by 27.72%. This study provides a theoretical foundation for the application of NBs in petroleum engineering and demonstrates significant potential for advancing efficient and environmentally sustainable oilfield development.

1. Introduction

Nanobubbles (NBs) possess an exceptionally long lifespan, remaining stable for days or even months. Their unique characteristics include a large specific surface area, strong adsorption capacity, and high mass transfer capabilities (Temesgen et al., 2017). These properties enable widespread applications in agriculture (Liu et al., 2016; Marcelino et al., 2023; Pal and Anantharaman, 2022), aquaculture (Dien et al., 2022; Lu et al., 2024; Yang et al., 2024), soil remediation (Ho et al., 2023; Kim and Han, 2020; Zhang et al., 2024b), groundwater treatment (Guo et al., 2025; Hu and Xia, 2018; Li et al., 2014), and mineral flotation (Li et al., 2025; Zhang et al., 2024a; Zinjenab et al., 2023). Based on the demonstrated efficacy of NBs in efficiently removing organic pollutants from water and soil (Bai et al., 2025; Wu et al., 2021; Xiao et al., 2025) and their ability to regulate solid-surface wettability (Jin et al., 2022; Ma et al., 2022), along with their characteristic of being produced solely through physical methods

* Corresponding author.
E-mail address: sllx_upc@126.com (J. Hou).
Peer review under the responsibility of China University of Petroleum (Beijing).

https://doi.org/10.1016/j.petsci.2026.03.015
1995-8226/

such as mechanical shearing, porous membrane-assisted aeration, and pressure cycling (Lu et al., 2022; Ushikubo et al., 2010; Wang and Wang, 2023) without requiring chemical additives. This technology demonstrates significant potential for development into a novel, environmentally friendly, and low-cost enhanced oil recovery technique. When CO_2 is selected as the gas source, this technology not only enhances crude oil recovery effectively but also achieves carbon sequestration, establishing an integrated approach that combines oil displacement with carbon sequestration.

Conventional CO_2 flooding can simultaneously enhance oil recovery and achieve carbon sequestration (Ajoma et al., 2020), but issues such as gas channeling (Zhao et al., 2020) and gravity override (Chen and Reynolds, 2018) often arise during the oil displacement process. These restrict the migration range of CO_2 within the reservoir, leaving vast oil-bearing pores inadequately mobilized. Moreover, the primary carbon sequestration mechanism in conventional CO_2 flooding relies on structural trapping, with relatively low contributions from solubility and mineral trapping. The long-term sequestration stability thus depends heavily on caprock integrity (Shukla et al., 2010), posing potential risks of CO_2 leakage due to geological activities (Bai et al., 2016). To address these challenges, the industry has developed several improved methods, including water-alternating-gas (WAG) injection (Abdulsada et al., 2025; Sarlak et al., 2021; Zhang et al., 2022) and CO_2 foam flooding by mixing CO_2, water, and surfactants (Chen et al., 2024; Tripathi et al., 2024; Zhang et al., 2015). However, these approaches still exhibit certain limitations. While WAG cannot fundamentally resolve gravity override issues, CO_2 foam demonstrates limited stability in high-temperature and high-salinity reservoirs, which restricts its plugging efficiency (Jia et al., 2023; Rognmo et al., 2018). Additionally, the size discrepancy between foam bubbles and reservoir pore throats leads to abrupt increases in injection pressure (Aarra et al., 2014). To address this, an alternative approach has been developed involving the dispersion of CO_2 in water to create a microscale CO_2−water dispersion system, leading to the emergence of CO_2 microbubble flooding technology (Jiang et al., 2019; Jia et al., 2025). Compared to foam, microbubbles possess substantially smaller sizes and larger inter-bubble distances, significantly reducing injection pressure requirements. The Jamin effect induced by microbubble migration through pore spaces increases flow resistance, effectively sealing high-permeability zones (Jia et al., 2024). However, micron-sized bubbles still face stability issues. Under the long-term influence of complex temperature and pressure environments in reservoirs, micron-sized bubbles are susceptible to buoyancy-driven rising and Ostwald ripening, which accelerate gas–liquid separation and lead to gas channeling. Furthermore, reservoirs contain extensive sub-micron and nanoscale pores hosting residual oil, and microbubbles struggle to penetrate these tiny pores to effectively recover residual oil within them. This limitation is particularly evident in low-permeability and tight reservoirs, which are typically characterized by abundant pores at sub-micrometer and nanometer scales. Dispersing CO_2 into nanoscale bubbles to form a nanoscale water–gas dispersion system can effectively resolve the issues mentioned above. NBs primarily exhibit random Brownian motion in aqueous environments (Lei et al., 2024), with negligible influence from gravity and minimal gas–water separation. Extensive studies indicate that NBs remain stable in water for significantly longer durations compared to microbubbles (Oh and Kim, 2017). The enormous specific surface area of NBs significantly enhances mass transfer efficiency, accelerates water–rock reactions, increases mineral sequestration ratios, and improves the long-term stability of CO_2 sequestration (Wang et al., 2025). Moreover, their nanoscale size enables them to penetrate microporous hosting residual oil (Rafryanto et al., 2024), effectively recover the residual oil within.

Currently, nanobubble (NB) flooding technology remains at an early exploratory stage. Systematic research on the oil displacement mechanisms of NBs is still limited, with only a small number of studies reporting their potential for enhancing oil recovery and preliminary insights into the mechanisms of crude oil mobilization by NBs. Li et al. (2023) provided a systematic review of the fundamental properties, preparation methods, and characterization techniques of CO_2 NBs, highlighting their significant potential for enhancing oil recovery and carbon sequestration. Taman et al. (2025) conducted CO_2 NB flooding experiments using glass micromodels and observed that NBs significantly expanded the sweep efficiency of the displacing fluid. The researchers attributed this effect to the interfacial activity of NBs, which includes reducing oil–water interfacial tension and forming adsorption layers on solid surfaces to decrease frictional resistance during crude oil flow. Elnaggar et al. (2025) demonstrated through core imbibition experiments that N_2 NB flooding significantly enhances oil recovery compared to pure water flooding, with a notably greater improvement observed in oil-wet cores than in water-wet cores. Wang et al. (2023) compared the cleaning effects of pure water and NB suspension on oil-contaminated sand and found that NBs significantly improved crude oil removal efficiency. The researchers attributed this enhancement to two mechanisms: NBs adsorbing onto the oil surface to promote its detachment from sand grains, and pressure waves generated by bubble collapse further accelerating the oil separation process from the sand surface. Zhu et al. (2025) utilized nuclear magnetic resonance technology to investigate the enhancement of oil recovery in conglomerate reservoirs using N_2 and CO_2 NBs. Their study revealed that NBs effectively address the low displacement efficiency caused by strong heterogeneity in conglomerate reservoirs. Compared to conventional water flooding, NB injection significantly improved oil recovery in these complex formations. Compared to conventional water flooding, NBs significantly enhanced oil recovery in conglomerate reservoirs.

Current research on the oil displacement mechanisms of NBs presents several critical issues warranting further investigation: On one hand, characterization of NB stability under realistic reservoir conditions (e.g., high temperature, high salinity, and other complex environments) remains insufficient; on the other hand, experimental and analytical studies of the flow behavior of NBs in porous media and their regulatory effects on oil–water relative permeability are notably lacking. These limitations hinder a comprehensive understanding of the mechanisms underlying NBs' enhanced oil recovery.

This study systematically investigates the mechanisms through which NBs enhance oil recovery and evaluate their potential applications in oilfield development. First, nanoparticle tracking analysis is utilized to evaluate the effects of external factors such as salinity and temperature on NB stability, revealing their stable characteristics under complex reservoir conditions. Subsequently, measurements of interfacial tension and contact angle, combined with oil film detachment experiments, are conducted to examine the influence of NBs on oil–water interfacial tension, solid surface wettability, and oil film detachment efficiency. These analyses help clarify the regulatory mechanisms by which NBs govern multiphase interfacial properties. Finally, multi-scale flow experiments in porous media and oil displacement tests are conducted to investigate the flow characteristics of NBs and their effects on oil–water relative permeability. Through a comprehensive analysis of the mechanisms by which NBs enhance oil recovery, this study provides theoretical support for the industrial application of NB flooding technology and promotes its large-scale implementation in petroleum development.

2. Materials and methods

2.1. Materials

The pure water used for NB preparation was laboratory-produced, and the high-purity CO_2 was obtained from Qingdao Deyi Gas Co., Ltd. High-purity NaCl, sodium dodecyl benzene sulfonate, and eosin Y (laboratory grade) were purchased from Sinopharm Chemical Reagent Co., Ltd. The solid substrate (glass coverslip) used for contact angle measurements was sourced from Jiangsu Shitai Laboratory Equipment Co., Ltd. Beakers and glass slides (25.4 mm × 76.2 mm) for oil film detachment experiments were sourced from Jiangsu Shitai Laboratory Equipment Co., Ltd. and Jiangsu Feizhou Glass & Plastic Products Co., Ltd., respectively. Artificial cores with a diameter of 2.5 cm and a length of 10 cm were used for core-scale flow and displacement experiments, with permeabilities of 33.9×10^{-3} and 340×10^{-3} μm^2. Fluorescent particles for single-channel particle image velocimetry (PIV) experiments were supplied by Thermo Fisher Scientific. Details of the simulated oil are provided in Table 1. Two types of microfluidic chips (Fig. 1) were employed: a single-channel chip (throat length: 400 μm) and a microfluidic porous media micromodel (coordination numbers (N_c): 3, 4, and 6 from right to left). The selection of these coordination numbers was based on literature-reported pore-throat connectivity distributions in natural sandstones, which are typically concentrated in the range of 2 to 6. The chosen values of 3, 4, and 6 lie within this high-frequency interval and therefore represent the most common pore-throat connectivity patterns encountered in actual reservoirs (Chen et al., 2019; Lin et al., 2024). Additional parameters are summarized in Table 2, and schematic diagrams are shown in Fig. 1.

2.2. Experimental setup

The nanoparticle tracking analyzer (Particle Metrix, ZetaView® Evolution, Germany) was used to determine the size, concentration, and zeta potential of NBs. A mechanical stirrer (SUNNE, SN-OES-100SH, China) was used to apply shear to the NBs. A smartphone (Honor, Magic5 Pro, China) was used to capture images during oil film detachment experiments. The contact angle goniometer (Biolin Scientific, Theta Flow, Sweden) was applied to measure interfacial tension and contact angles. The atomic force microscope (AFM) (Oxford Instruments, Cypher ES, UK) was used to obtain the topography and surface roughness of the solid surface with adsorbed NBs. The NB generation device is shown in Fig. 2, which primarily consists of a CO_2 gas cylinder (diameter 235 mm, height 1400 mm), a gas injection pipeline (outer diameter 6 mm, inner diameter 4 mm), a circulation pump (ZKSJ, DC55E-24160A, China), a NB generator (Zhuhong Nano, ZH0100, China), a water circulation pipeline (outer diameter 10 mm, inner diameter 8 mm), and a water container (diameter 150 mm, height 800 mm).

The microfluidic and PIV flow field velocimetry device is shown in Fig. 3(a). It consists of a fluid injection system, an image acquisition system, and a PIV system. The injection system includes a micro-injection pump (Harvard Apparatus, PHD, 2000, USA), syringes (Hamilton, USA), PTFE tubing (1/16 inch), and a microfluidic chip. The image acquisition system comprises a high-magnification optical microscope (Photron, SAZ, Japan) and a high-resolution camera. The PIV system is equipped with a laser emitter (Litron Lasers, UK) and optical fibers. The micro-injection pump operated at flow rates ranging from 76 nL/min to 79 mL/min, and the high-speed camera captured images at 2000 fps. The core flooding experimental device is shown in Fig. 3(b), which mainly includes a high-pressure precision plunger pump (Teledyne ISCO, Series D, USA), intermediate containers, a six-way valve, a pressure gauge (Asmik, Y190, China), a core holder, a hand-operated pump, and associated tubing.

Table 1
Detailed information on experimental simulation oils.

Experiment name	Composition of simulated oil	Viscosity, mPa·s
Interfacial tension and contact angle	Crude oil and kerosene	25
Oil film detachment experiment	Crude oil and kerosene	1024
Microscopic displacement	Silicone oil	350
Relative permeability test	Crude oil and kerosene	25
Core flooding experiment	Crude oil and kerosene	25

2.3. Experimental procedure

The experimental procedure is illustrated in Fig. 4, which presents the overall experimental scheme, methodologies employed, and research purposes of this study. The specific steps and operational details of each experiment will be described individually in the following sections.

2.3.1. Characterization of fundamental NB properties

To characterize the fundamental properties of NBs, NBs were first prepared according to the following procedure: The gas cylinder valve was opened, and the gas inlet pressure of the NB generator was set to 0.1 MPa. The circulation pump was operated at full power (80 W) for 30 min, followed by a standing period to allow the dissipation of millimeter-sized and micrometer-sized bubbles in the solution. The size and concentration of the NBs under different salinity, temperatures, and aging times, as well as the zeta potential under varying salinity and aging times, were measured using a nanoparticle tracking analyzer to evaluate their salt tolerance, thermal stability, and temporal stability. Additionally, the NBs were subjected to shear treatment using a mechanical stirrer at different rotation speeds and durations. The size and concentration after shear application were measured with the nanoparticle tracking analyzer to assess their shear resistance. All aforementioned measurements were conducted in triplicate to ensure reproducibility. The detailed experimental design is provided in Table 3.

Table 2
Detailed parameters of microfluidic chips.

Experiment name	Microfluidic chip material	Throat etching aperture, μm	Throat etching depth, μm	Pore etching aperture, μm	Pore etching depth, μm
PIV flow field test	PDMS	100	100	500	500
Microscopic displacement experiment	SiO_2	50	200	50	300

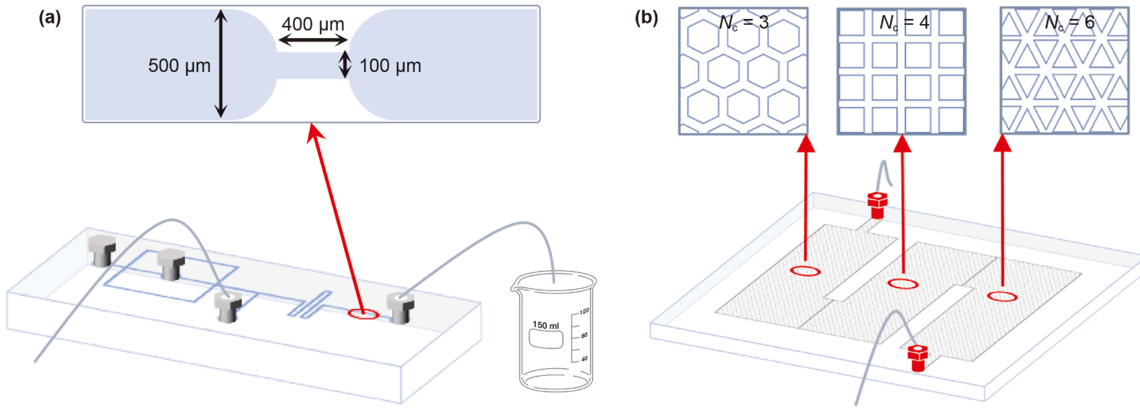

Fig. 1. Schematic diagram of microfluidic chips. (**a**) Single-channel chip; (**b**) microfluidic porous media micromodel.

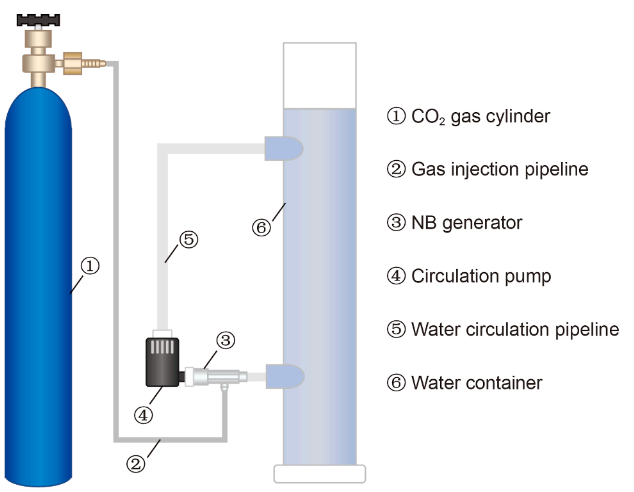

Fig. 2. NB generation device.

2.3.2. NB interfacial properties

The effect of NBs on interfacial properties were investigated by measurements the dynamic oil–water interfacial tension and under-liquid contact angles. All measurements were conducted at 25 °C and under ambient atmospheric pressure using a contact angle goniometer. The NB suspension (prepared as described in Section 2.3.1, with a concentration of 1.5×10^7 particles/mL and a mean particle size of 186 nm) and pure water were used as the aqueous phase. Dynamic interfacial tension between crude oil and each aqueous phase was recorded over a period of 600 s. For contact angle measurements, SiO_2 coverslips served as the solid interface. The obtained interfacial tension and contact angle values for the NB suspension were then compared with those for pure water to elucidate the role of NBs.

AFM testing was conducted using the liquid-tapping mode for in-situ imaging of the solid surface to obtain its micro-topography and roughness. The specific procedure is as follows: First, a clean glass coverslip was immersed in pure water, and after 1 min of immersion, its surface topography was scanned (scan area 2 μm × 2 μm) and the root mean square roughness was calculated. Subsequently, while keeping the sample position unchanged, the immersion medium was replaced with a NB suspension, and after continuing immersion in the same area for 1 min, scanning imaging was performed again to obtain the surface topography under this condition and the corresponding root mean square roughness was calculated.

Oil film detachment experiments were conducted using different reagents, as schematically illustrated in Fig. 5. Specifically, 1.5 mL of crude oil was deposited onto a glass slide and uniformly spread to cover three-quarters of the slide surface, forming an oil film with a height of 57.2 mm and a width of 25.4 mm. The slide was then immersed in beakers containing different reagents, with the liquid level consistently adjusted to fully submerge the oil-coated area. The immersion reagents included an NB suspension (1.5×10^7 particles/mL, a mean particle size of 186 nm), a surfactant solution (0.1 wt% sodium dodecyl benzene sulfonate), and pure water. Images of the oil film were captured at immersion times of 1, 5, 10, 15, and 20 min. The acquired images were preprocessed using image processing software to remove irrelevant regions and correct perspective distortion. Subsequently, ImageJ was employed to segment the oil-covered and bare regions, and the pixel counts of both areas were quantified. The oil coverage ratio and oil film detachment rate were calculated as follows:

$$P_{OA} = \frac{n_o}{n_o + n_b} \times 100\% \tag{1}$$

$$v_o = \frac{P_{OA1} - P_{OA2}}{t_2 - t_1} \times 100\% \tag{2}$$

where P_{OA} is the oil coverage ratio, %; n_o is the pixel count of the oil-covered region; n_b is the pixel count of the blank region; v_o is the oil film detachment rate, %/min; t_1 and t_2 are two time points during oil film immersion, min; and P_{OA1} and P_{OA2} are the corresponding oil coverage ratios at t_1 and t_2, respectively.

2.3.3. PIV velocity measurement experiment

PIV velocity measurements were conducted in a single-channel constricted pore throat to compare the flow fields of pure water and the NB suspension. The NB suspension was prepared using pure water as the base fluid, as described in Section 2.3.1, and had a concentration of 1.5×10^7 particles/mL with a mean particle size of 186 nm.

The PIV technique measures fluid velocity by tracking the displacement of seeded particles. Fluorescent tracer particles are added to the fluid (water or NB suspension). As the fluid flows through the microchannel, a laser sheet illuminates these particles, and their motion is captured through a microscope by a high-speed camera. The displacement of particle patterns between consecutive images is then analyzed via a cross-correlation

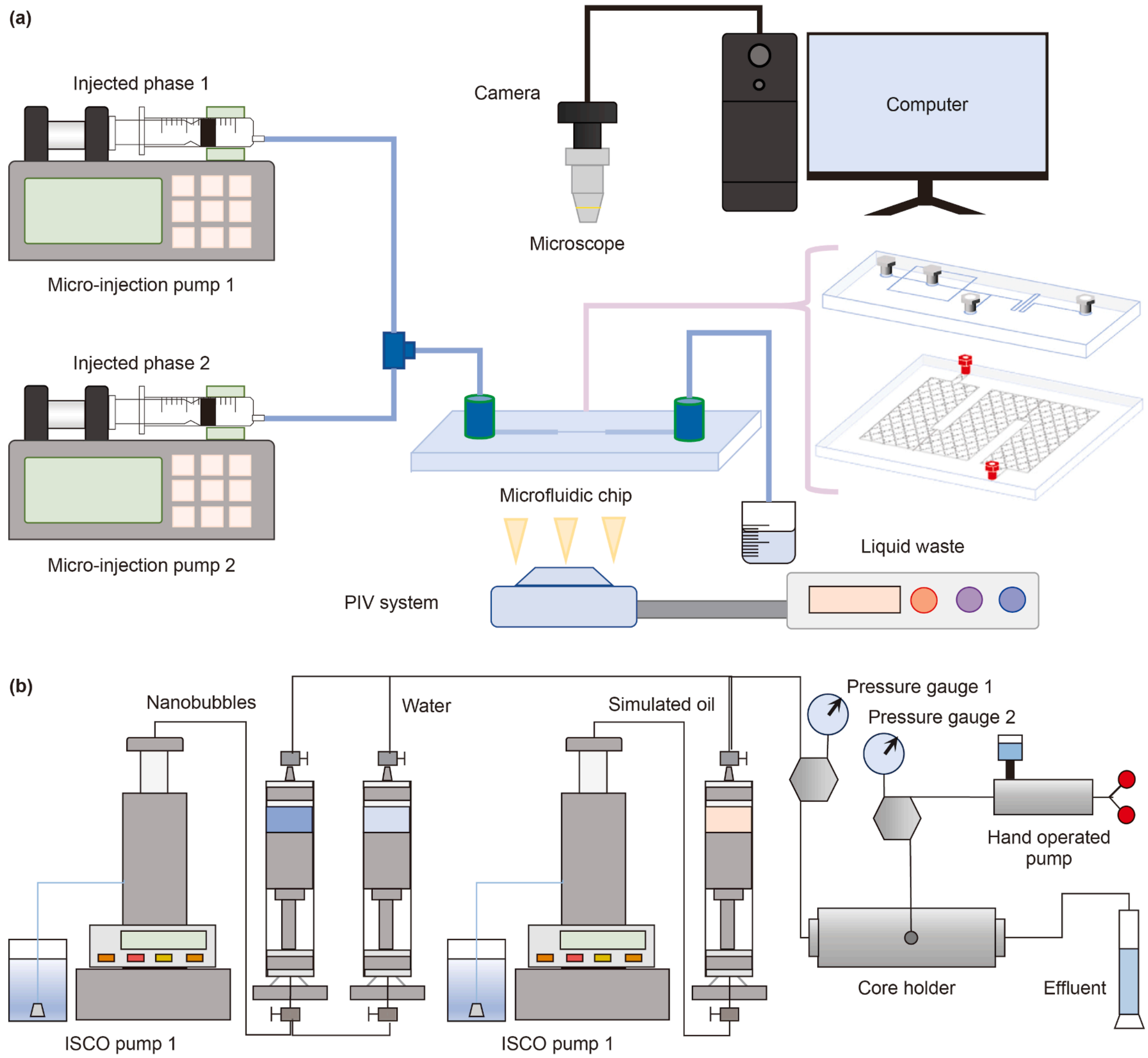

Fig. 3. Schematic diagrams of experimental setups. (**a**) Microfluidic and PIV flow field velocimetry setup; (**b**) core flooding apparatus.

algorithm to calculate the velocity field. The experimental procedure was as follows. First, fluorescent tracer particles (1 wt%) were added to both the water and NB suspension and the mixtures were oscillated to achieve uniform dispersion. Prior to injection, the microfluidic chip was pre-flushed with pure water to eliminate air bubbles and prevent experimental interference. Under the white-light mode, the microscope and chip position were adjusted to ensure the observation area was clearly centered in the field of view. The water or NB suspension was then injected into the chip at a flow rate of 10 μL/min using a micro-injection pump. After switching the PIV system to laser mode, the grid pixels were set to 32 × 32, and the camera capture interval was adjusted to ensure approximately 8 particles per grid and a particle displacement of 1/4–1/2 grid length between consecutive images. Once the flow stabilized, 20 images of fluorescent particle movement were captured to define the analysis region, followed by another 20 images for detailed analysis. The images were processed using an adaptive cross-correlation algorithm to calculate velocity vectors within the grid regions, and particle displacements were used to determine the flow field. Median filtering was applied to remove noise, and vector statistics from the 20 images were averaged to generate a mean flow field map. After the experiment, the microchannel was thoroughly flushed to remove any residual fluorescent particles and bubbles. The resulting flow field maps were analyzed to evaluate the influence of NBs on the flow behavior within the constricted pore throat.

2.3.4. *Core-scale flow experiment*

Core-scale flow experiments through porous media were conducted using a NB suspension to analyze its flow characteristics. The NB suspension, prepared with pure water as the base fluid as described in Section 2.3.1, had a concentration of 1.5 × 10^7 particles/mL and a mean particle size of 186 nm. The experiments were performed at 25 °C, with the outlet maintained at atmospheric pressure. The permeabilities of the cores used in the experiments were 33.9 × 10^{-3} and 340 × 10^{-3} μm^2, respectively.

The experimental procedure was as follows: Water and the NB suspension were loaded into separate intermediate containers. The pore volume of the core was determined using the gravimetric method. The core was placed in a core holder, and a confining pressure of 2 MPa was applied using a hand pump. The valves were adjusted to allow the ISCO pump to inject water into the core at a flow rate of 0.1 mL/min for 1 pore volume (PV), followed by injection of the NB suspension at the same flow rate and the same volume (1 PV). Throughout the injection process, pressure readings at the inlet of the core holder were continuously recorded, and the pressure differential across the core was monitored.

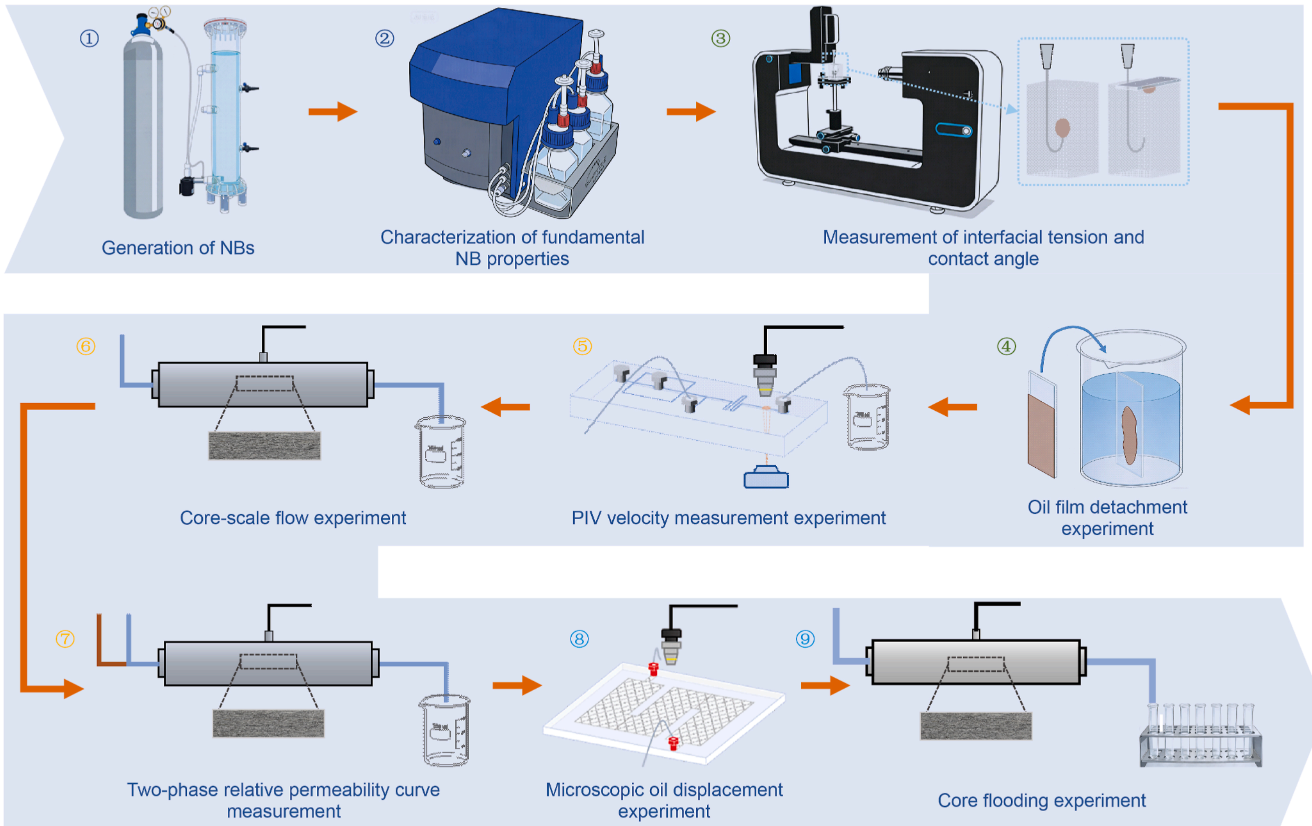

Fig. 4. Overview of experimental research procedure.

Table 3
Experimental scheme for characterizing the basic properties of NBs.

NB stability	Salinity, 10^3 mg/L	Temperature, °C	Rotation speed, r/min	Shearing time, min	Aging time, d
Control group	0	25	/	/	1
Salt resistance	1	25	/	/	1
	5	25	/	/	1
	10	25	/	/	1
	15	25	/	/	1
	20	25	/	/	1
	30	25	/	/	1
Thermal stability	5	45	/	/	1
	5	65	/	/	1
	5	85	/	/	1
Shear resistance	5	25	200	30	1
	5	25	500	30	1
	5	25	200	120	1
Temporal stability	0	65	/	/	1
	0	65	/	/	2
	0	65	/	/	3
	0	65	/	/	4
	0	65	/	/	5

2.3.5. Two-phase relative permeability curve measurement

The oil–water/NB suspension two-phase relative permeability curves were measured to investigate the effect of NBs on relative permeability. The NB suspension, prepared with pure water as the base fluid as described in Section 2.3.1, had a concentration of 1.5×10^7 particles/mL and a mean particle size of 186 nm. The experiments were performed at 25 °C, with the outlet maintained at atmospheric pressure. The permeabilities of the cores used in the experiments were 33.9×10^{-3} μm^2.

The experimental procedure was as follows: The core sample was cleaned, and water, NB suspension, and simulated oil were loaded into separate intermediate containers. The pore volume of the core was determined using the gravimetric method. The core was placed in a core holder, and a confining pressure of 2 MPa was applied using a hand pump. The valve configuration was adjusted to allow ISCO pump 1 to inject water into the core at a flow rate of 0.1 mL/min for 5 PV. This was followed by simulated oil flooding at the same flow rate (0.1 mL/min). During oil flooding, the produced fluids were collected in graduated cylinders, which were replaced every 10 min. The volumes of oil and water produced were recorded to calculate the water cut. When the water cut reached zero, the injection of simulated oil was stopped, indicating complete saturation of the core with oil and establishment of irreducible water saturation. The cumulative water production was calculated, and the irreducible water saturation was determined using the following formula:

$$S_{wi} = \frac{V_p - V_w}{V_p} \tag{3}$$

where S_{wi} is the irreducible water saturation; V_p is the pore volume of the core, cm^3; V_w is the cumulative water production, cm^3.

After saturating the core with simulated oil, it was allowed to stand for 4 h. Subsequently, simulated oil was injected into the core at a flow rate of 0.1 mL/min. Once the flow stabilized (indicated by the injection of more than 3 PV of simulated oil and a stable pressure differential across the core), the pressure difference was recorded, and the injection was stopped. The effective permeability of the oil phase at irreducible water saturation was calculated using the following formula:

$$k_{o\text{-}wi} = \frac{q_o \mu_o L}{A \Delta p} \times 10^{-1} \tag{4}$$

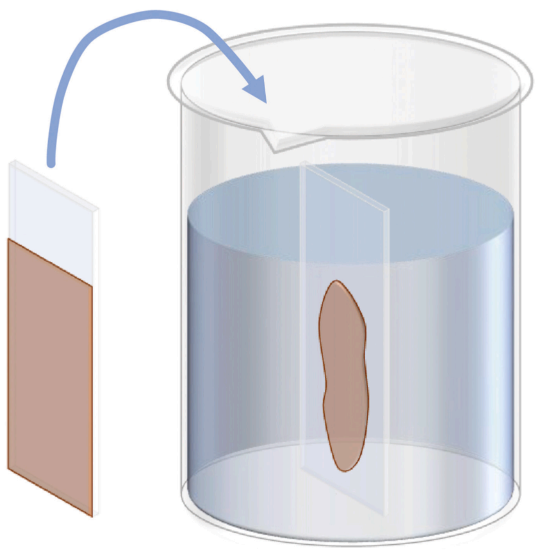

Fig. 5. Schematic diagram of the oil film detachment experiment.

where $k_{o\text{-}wi}$ is the effective permeability of the oil phase at irreducible water saturation, μm^2; q_o is the flow rate of simulated oil, cm^3/s; μ_o is the viscosity of simulated oil, mPa·s; L is the length of the core, cm; A is the cross-sectional area of the core, cm^2; and Δp is the pressure difference across the core, MPa.

Subsequently, while maintaining a constant total flow rate, simulated oil and water/NB suspension were co-injected into the core at predetermined ratios (20:1, 10:1, 5:1, 1:1, 1:5, 1:10, and 0:1). After flow stabilization (indicated by the injection of more than 3 PV of both fluids and a stable pressure differential across the core), the mass of the core was measured, and the pressure difference as well as the flow rates of simulated oil and water/NB suspension were recorded. The water saturation was determined gravimetrically, and the relative permeabilities of simulated oil and water/NB suspension were calculated using the following formulas:

$$S_w = \frac{m_i - m_0 - \rho_o V_p}{V_p(\rho_w - \rho_o)} \tag{5}$$

$$k_w = \frac{q_w \mu_w L}{A \Delta p} \times 10^{-1} \tag{6}$$

$$k_o = \frac{q_o \mu_o L}{A \Delta p} \times 10^{-1} \tag{7}$$

$$k_{rw} = \frac{k_w}{k_o(S_{wc})} \tag{8}$$

$$k_{ro} = \frac{k_o}{k_o(S_{wc})} \tag{9}$$

where S_w is the water saturation; m_i is the mass of the core after co-injection of simulated oil and water/NB suspension at a specific ratio and upon achieving flow stabilization, g; m_0 is the initial mass of the core before fluid injection, g; ρ_o is the density of the simulated oil, g/cm^3; ρ_w is the density of water/NB suspension, g/cm^3; q_w is the flow rate of water/NB suspension, cm^3/s; μ_w is the viscosity of water/NB suspension, mPa·s; k_w is the effective permeability of water/NB suspension, μm^2; k_o is the effective permeability of the simulated oil, μm^2; k_{rw} is the relative permeability of water/NB suspension; and k_{ro} is the relative permeability of simulated oil. Based on these data, the oil-water/NB suspension two-phase relative permeability curves were plotted.

2.3.6. Microscopic oil displacement experiment

Microscopic oil displacement experiments were conducted using pure water and NB suspension to compare their displacement efficiencies. The NB suspension, prepared with pure water as the base fluid as described in Section 2.3.1, had a concentration of 1.5×10^7 particles/mL and a mean particle size of 186 nm. The experiments were performed at 25 °C, with the outlet maintained at atmospheric pressure. The experimental procedure was as follows: First, both water and NB suspension were dyed with 0.5 wt% eosin Y. The microfluidic porous media micromodel was thoroughly cleaned. Simulated oil was drawn into a syringe and injected into the microfluidic chip at a flow rate of 50 μL/min until the chip was fully saturated with oil. Then, the dyed water or NB suspension was loaded into a syringe and injected into the chip at the same flow rate (50 μL/min). After the displacement process, images of the oil and water/NB distribution were recorded. ImageJ was used to segment oil-containing and water/NB-containing pores, and the sweep efficiencies of water/NB suspension in regions with different coordination numbers were calculated.

2.3.7. Core flooding experiment

Core flooding experiments were conducted using pure water and NB suspension to compare their oil displacement efficiencies. The NB suspension, prepared with pure water as the base fluid as described in Section 2.3.1, had a concentration of 1.5×10^7 particles/mL and a mean particle size of 186 nm. The experiments were performed at 25 °C, with the outlet maintained at atmospheric pressure. The permeabilities of the cores used in the experiments were 33.9×10^{-3} and 340×10^{-3} μm^2, respectively. The experimental procedure was as follows: Water, NB suspension, and simulated oil were loaded into separate intermediate containers. The PV of the core was determined gravimetrically. The core was placed in a core holder, and a confining pressure of 2 MPa was applied using a hand pump. The valves were adjusted to allow ISCO pump 1 to inject water into the core at a flow rate of 0.1 mL/min for 5 PV, followed by ISCO pump 2 injecting simulated oil at 0.1 mL/min for 4 PV to achieve core saturation with oil. The valves were then reconfigured to inject water at 0.1 mL/min to displace the oil. Produced fluids were collected in graduated cylinders, which were replaced every 10 min. The volumes of oil and water were measured to calculate the water cut and cumulative recovery ratio. Water injection was stopped when the water cut reached 98%. Subsequently, the valves were adjusted to allow ISCO pump 1 to inject NB suspension at 0.1 mL/min for oil displacement. Similarly, produced fluids were collected and measured every 10 min to calculate the water cut and cumulative recovery ratio. The process was terminated when the water cut reached 98%. Throughout the displacement process, the pressure at the inlet of the core holder was continuously recorded. To ensure the repeatability of the oil recovery enhancement achieved by NBs, triplicate parallel core flooding tests were conducted for each permeability condition.

3. Result and discussion

3.1. NB stability

3.1.1. Salt resistance

The dark-field scattering microscopy image of NBs, acquired during size and concentration measurement using nanoparticle tracking analysis (NTA), is presented in Fig. 6(a). A laser beam was

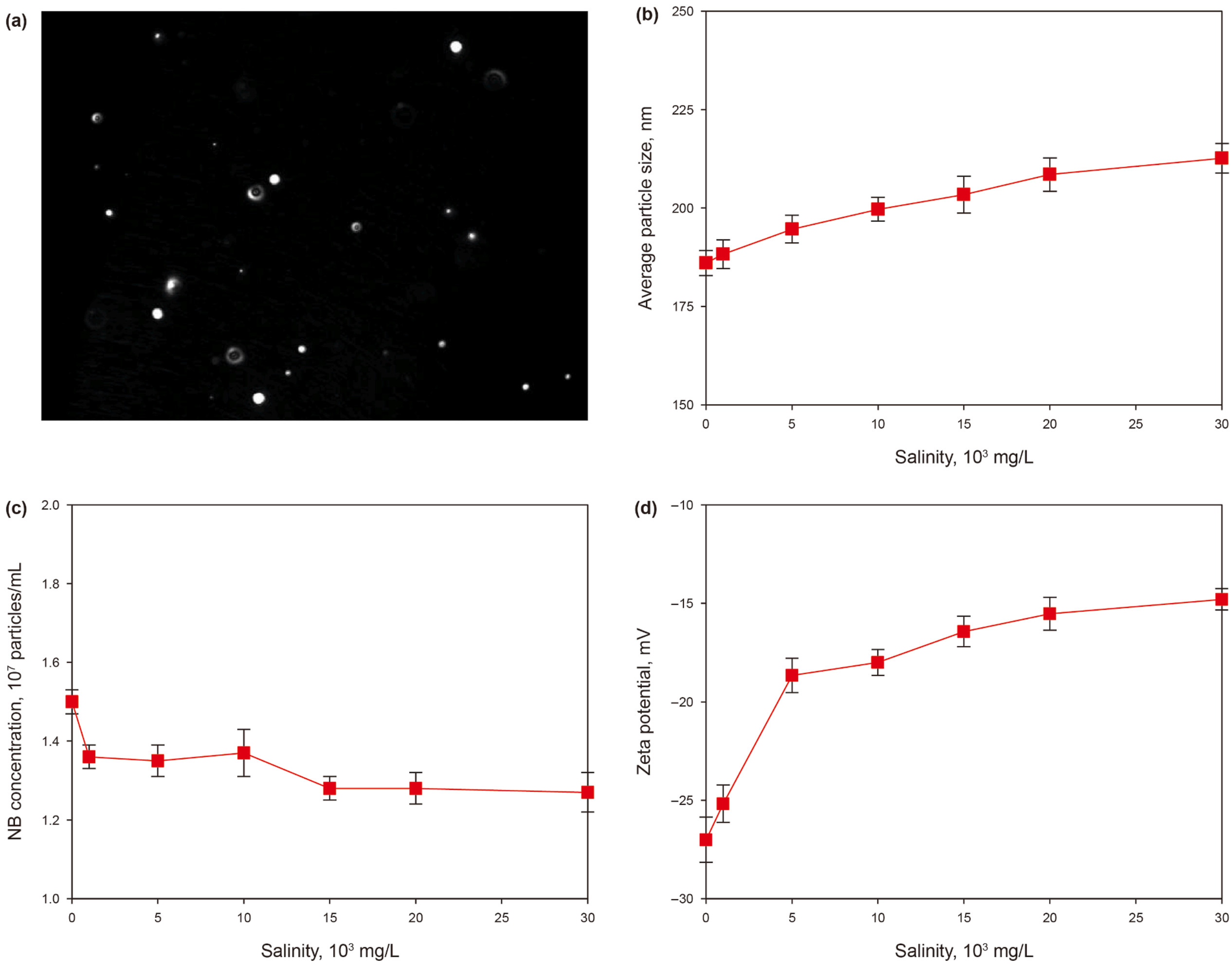

Fig. 6. Dark-field scattering microscopic image of NBs (**a**) and the influence of salinity on the concentration (**b**), particle size (**c**), and zeta potential (**d**) of NBs.

illuminated laterally through the sample cell containing NBs, and the scattered light from the NBs was captured by a camera, forming bright spots against a dark background. Each bright spot corresponds to an individual NB. By analyzing the Brownian motion trajectories and light intensity distributions of these spots, the size and concentration of the NBs were quantitatively determined.

The average size and concentration of NBs under varying salinity are shown in Fig. 6(b, c), respectively. As the salinity increased from 0 to 30 $\times$ 10^3 mg/L, the average size of NBs exhibited a limited upward trend, growing from an initial value of 186 to 212.7 nm, representing an increase of 14.35%. This observed increase in bubble size with rising salinity aligns with trends reported in prior studies of NB colloidal stability under saline conditions (Agarwal et al., 2022; Ke et al., 2019; Ma et al., 2024). Conversely, the NB concentration showed a limited downward trend, yet remained on the order of 10^7 particles/mL, decreasing from an initial value of 1.5 $\times$ 10^7 to 1.27 $\times$ 10^7 particles/mL, corresponding to a reduction of 15.33%. The zeta potential of NBs under varying salinity is displayed in Fig. 6(d). The results indicate that NBs carry negative surface charges, and the absolute value of their zeta potential decreased with increasing salinity, dropping from an initial value of 27 to −14.8 mV. According to DLVO theory, as the salinity increases, the concentration of counter-ions (e.g., Na^+) in the solution rises, compressing the electric double layer on the NB surface. This reduces the absolute zeta potential of the NBs, weakening the electrostatic repulsion between them and compromising their colloidal stability. Under the influence of van der Waals forces, some NBs aggregated and coalesced, leading to the observed increase in average size and a slight decrease in concentration. However, even at salinity of 30 $\times$ 10^3 mg/L, the changes in average size and concentration were relatively small, and the absolute zeta potential remained at 14.8 mV. This combination of properties demonstrates the relatively strong salt tolerance of NBs.

3.1.2. Thermal stability

The average size of NBs at different temperatures is shown in Fig. 7(a). As the temperature increased from 25 to 85 °C, the average NB size exhibited a growing trend, rising from an initial value of 193.63 to 306.05 nm, with an increase of 58.1%. The concentration of NBs at different temperatures is presented in Fig. 7(b). The NB concentration first increased and then decreased with rising temperature, peaking between 45 and 65 °C.

This behavior can be attributed to the reduced solubility of CO_2 at higher temperatures, leading to the release of dissolved CO_2. Part of the released gas migrated into existing NBs, causing them to expand and increasing the average size, while another portion underwent homogeneous nucleation, forming new NBs and temporarily elevating the concentration. As the temperature continued to rise, the intensified thermal motion of liquid molecules enhanced the Brownian movement of NBs, significantly increasing the frequency of collisions between them. When the thermal energy exceeded the stability barrier of the system, the probability of NB aggregation greatly increased, accelerating

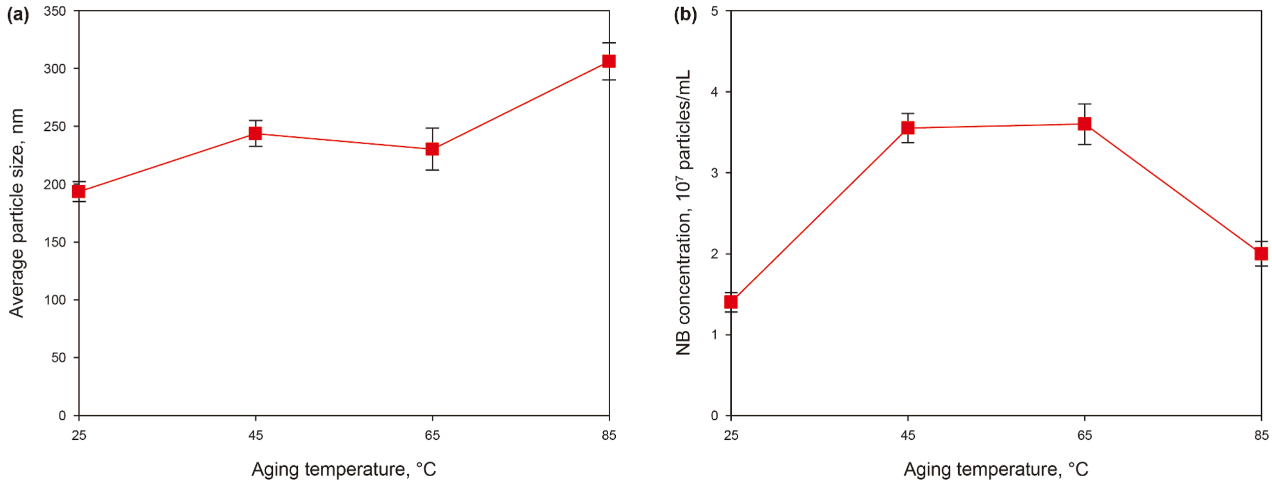

Fig. 7. The influence of aging temperature on the particle size (**a**) and concentration (**b**) of NBs.

Ostwald ripening and resulting in further growth in average size and a decline in concentration. Despite the increase in average size at elevated temperatures, the average diameter of NBs remained around 300 nm even at 85 °C. Moreover, rather than causing a decrease in concentration, higher temperatures led to a noticeable rise in NB concentration at 45 and 65 °C. These results demonstrate that the NB system exhibits favorable temperature tolerance.

3.1.3. Temporal stability

The average size and concentration of NBs at different aging times are shown in Fig. 8. As the aging period extended from 1 to 5 d, the average NB size fluctuated within the range of 220–250 nm, while the concentration varied between 2.7×10^7 and 3.6×10^7 particles/mL. The absolute zeta potential remained stable at approximately 15 mV. These results demonstrate that NBs maintain excellent temporal stability even in the absence of surfactants. This stability primarily arises from two mechanisms: the electrostatic repulsion generated by surface charges on the NBs, which inhibits coalescence and retards Ostwald ripening, and the sustained Brownian motion, which effectively counteracts the buoyancy-driven upward migration of NBs.

3.1.4. Shear resistance

The average size and concentration of NBs after shear treatment at different rates and durations are shown in Fig. 9. When the shear time was fixed at 30 min, an increase in the shear rate to 500 r/min reduced the average NB size from 186 to 169 nm (a decrease of 8.6%), while the NB concentration increased from 1.5×10^7 to 1.7×10^7 particles/mL (an increase of 13.3%). When the shear rate was fixed at 200 r/min, extending the shear duration to 120 min decreased the average size from 186 to 158 nm (a reduction of 15.1%), with the concentration similarly rising from 1.5×10^7 to 1.7×10^7 particles/mL (an increase of 13.3%). These results demonstrate the strong shear resistance of NBs, which is attributed to the electrostatic repulsion generated by their surface charges, effectively suppressing bubble coalescence. Concurrently, mechanical shear promotes the fragmentation of larger bubbles into smaller ones, leading to a moderate reduction in the average size and a corresponding increase in concentration within the system.

3.2. NB interfacial properties

3.2.1. Interfacial tension and contact angle

The temporal evolution of interfacial tension between oil and water/NB suspension measured by the pendant drop method is shown in Fig. 10(a), with a total measurement duration of 600 s. During the initial stage (0–200 s), the interfacial tension of the oil–water/NB suspension exhibited a significant decreasing trend over time. As the test progressed into the mid-to-late stage (200–600 s), the interfacial tension gradually stabilized with further extension of time. The final interfacial tension between oil

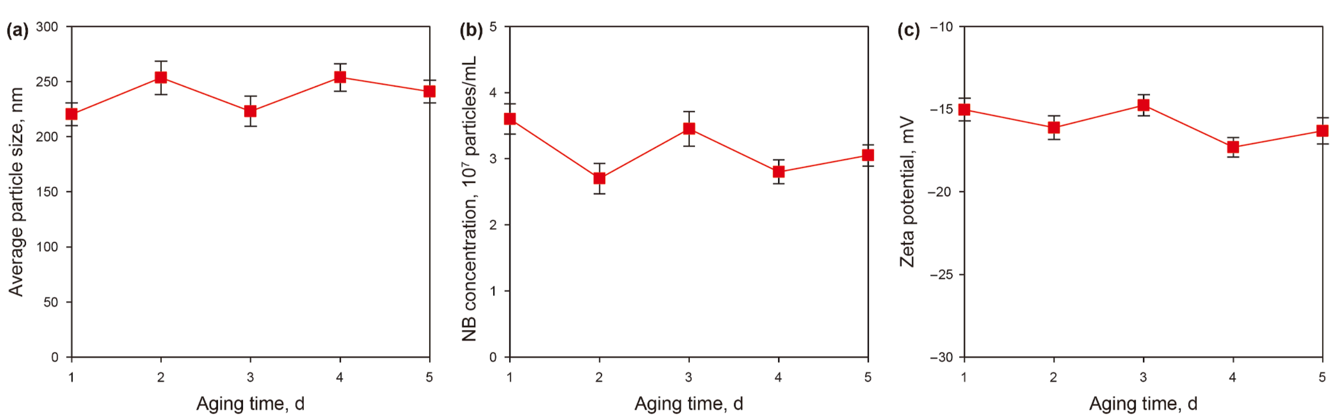

Fig. 8. The influence of aging time on the particle size (**a**), concentration (**b**), and zeta potential (**c**) of NBs.

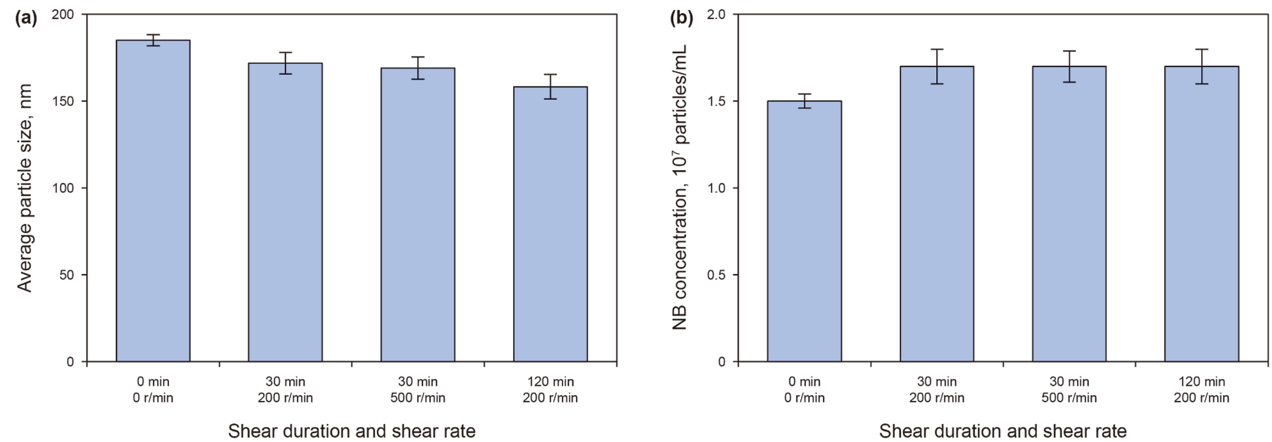

Fig. 9. The influence of shear duration and shear rate on the particle size (**a**) and concentration (**b**) of NBs.

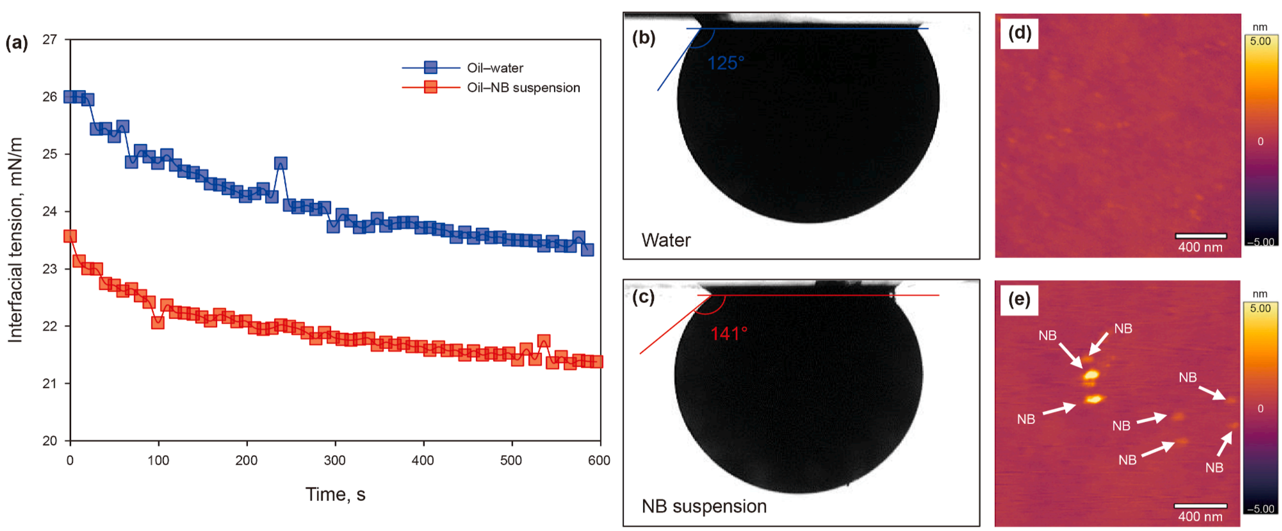

Fig. 10. Interfacial tension and contact angle measurements, and microscopic topography of the glass coverslip surface. (**a**) Interfacial tension of oil–water/NB suspension; (**b**) underwater contact angle of crude oil in pure water; (**c**) underwater contact angle of crude oil in NB suspension; (**d**) surface topography of the glass coverslip after immersion in pure water; (**e**) surface topography of the glass coverslip after immersion in NB suspension.

and water decreased from 26 to 23.33 mN/m (a reduction of 2.67 mN/m), while that between oil and NB suspension decreased from 23.57 to 21.38 mN/m (a reduction of 2.19 mN/m). This behavior can be attributed to the gradual adsorption of natural active components from the oil phase onto the interface, which modifies the interfacial composition and reduces interfacial tension. The adsorbed molecules also require time for conformational rearrangement, leading to a further decrease in interfacial tension. Once the interfacial composition stabilized, the interfacial tension gradually reached a steady state. Throughout the measurement process, the interfacial tension between oil and NB suspension remained consistently lower than that between oil and water. This reduction can be attributed to the adsorption of NBs at the oil–water interface and the formation of a surface excess, which leads to the partial replacement of the high-interfacial-energy oil–water contact area with a lower-interfacial-energy gas–oil contact region, thereby decreasing the overall interfacial tension (Agarwal et al., 2023; Tuziuti et al., 2023; Yang et al., 2023). Additionally, the Brownian motion and collapse of NBs generate localized microflows near the interface (Zhang et al., 2025). This disturbance enhances the exchange and rearrangement of molecules at the oil–water interface, accelerating the adsorption and enrichment of surface-active components. These two mechanisms synergistically contribute to the enhanced interfacial tension reduction by NBs.

The under-liquid contact angle test results between crude oil and glass coverslips are shown in Fig. 10(b, c). The under-liquid contact angle of crude oil in water was 125°, while that in the NB suspension was 141°. This indicates that the presence of NBs significantly enhanced the oleophobicity of the glass slide surface, increasing the contact angle by 16°. This phenomenon is primarily caused by the synergistic action of the following two mechanisms. First, the negative charges carried on the surface of the NBs, after adsorbing onto the glass slide surface, electrostatically repel the polar components in the crude oil, driving the contraction of the oil–water–solid three-phase contact line. Second, AFM characterization results show (Fig. 10(d, e)) that the adsorption of NBs forms discrete nanoscale gaseous protrusions on the solid surface, increasing the root mean square roughness from 0.215 to 0.325 nm, thereby creating a gas–solid composite interface. According to the Cassie-Baxter model, these gaseous protrusions act as “gas cushions”, causing some of the high-interfacial-energy solid–oil contact areas to be replaced by low-interfacial-energy gas–oil contact areas, thereby energetically suppressing the spreading tendency of the crude oil. The synergistic effect of the aforementioned electrostatic repulsion and the gas–solid composite interface ultimately manifests macroscopically as an increase in the contact angle.

Although the changes in interfacial tension and contact angle appear limited, they jointly regulate two key parameters affecting oil mobilization: the adhesion work and capillary pressure. On one hand, alterations in these interfacial parameters lead to a reduction in the adhesion work, directly weakening the adhesion of crude oil to the rock surface. This facilitates the transformation of residual oil from a fixed state into mobile droplets, thereby improving displacement efficiency. On the other hand, these changes enhance the capillary pressure, which serves as a driving force for oil displacement in the hydrophilic system. This promotes more effective imbibition of the displacing fluid into micropores, delays its channeling through larger pore pathways, helps stabilize the displacement front, and reduces the residual oil saturation in tiny pores.

3.2.2. Oil film detachment experiment

The morphological evolution of the oil film, the oil coverage ratio, and the oil film detachment rate over time during immersion in NB suspension and pure water are shown in Fig. 11(a, c–e). The following trends were observed: As the immersion time increased, the oil film area decreased in both liquid environments, and the oil-covered area ratio consistently declined. Notably, NBs significantly enhanced oil film detachment. After 20 min of immersion, the oil-covered area ratio decreased by up to 83.38% in the NB suspension, compared to only 19.7% in pure water under the same conditions, demonstrating the remarkable efficacy of NBs in accelerating oil film removal. Further analysis of the detachment process revealed that the detachment rate peaked immediately after the oil film contacted the liquid phase and then slowed as the interfacial composition stabilized. Overall, the detachment rate gradually decreased over time in both liquids. However, during the early and middle stages of immersion, the detachment rate in the NB suspension was significantly higher than that in pure water, with the peak detachment rate in NB suspension being four times that in water. NBs promote oil film detachment through multiple synergistic mechanisms, primarily involving interfacial property modulation and dynamic disturbances. NBs reduce oil–water interfacial tension and increase the contact angle between crude oil and the glass surface, thereby decreasing the adhesion work of crude oil on the glass. NBs adsorbed on the oil film surface generate micro-scale perturbations via continuous Brownian motion, while the collapse of some bubbles induces local fluid flow, collectively promoting oil film fragmentation. Additionally, NBs compete with the oil film for adsorption sites on the glass surface, further weakening the bonding strength between the oil film and the substrate. The synergy of these physicochemical effects ultimately enables highly efficient oil film detachment by NBs.

After immersing the oil film in pure water for 20 min and subsequently transferring it to a NB suspension for an additional 20 min, the morphological changes, oil-covered area ratio, and oil film detachment rate at different time points during the entire process are shown in Fig. 12. It can be observed that when the oil film was immersed in the NB suspension, the detachment rate increased from 0.35 to 11.59 %/min, with an increase of 32 times. Simultaneously, the oil-covered area ratio decreased from 80.3% to 6.73%, with a reduction of 73.57%. These results further demonstrate the significant promoting effect of NBs on oil film detachment, which is achieved through the synergistic combination of their unique interfacial activity and dynamic disturbance characteristics, enabling efficient oil removal.

To further explain the applied relevance of this study, a surfactant control group represented by 0.1 wt% sodium dodecyl benzene sulfonate was included in the experiments, aiming to comparatively reveal the performance differences and advantages between NBs and traditional chemical flooding agents. The temporal changes in the evolution of the oil film, the oil coverage ratio, and the oil film detachment rate in the surfactant solution are shown in Fig. 11(b, d, e). The experimental results indicated that during the initial immersion period (0–5 min), the decreasing trend in the oil coverage ratio in the surfactant solution was similar to that in the pure water system. As the immersion time extended, the detachment of the oil film in the surfactant solution gradually accelerated, and after 20 min of immersion, the oil coverage ratio was significantly lower than that in pure water, demonstrating that the surfactant had a stronger oil film detachment effect than pure water. However, compared to the NB suspension, the oil coverage ratio in the surfactant solution after 20 min remained higher, indicating that within the 20-min period, its detachment effect was weaker than that of the NB suspension. In terms of the oil film detachment rate, unlike the decreasing trends observed in pure water and the NB suspension, the oil film detachment rate in the surfactant solution gradually increased over time. At 15 min of immersion, the oil film detachment rate in the surfactant solution was lower than that in the NB suspension; after 15 min, the former surpassed the latter. These results indicate that within a shorter time scale (20 min), the NB suspension outperforms the surfactant solution in oil film detachment. However, based on the trend of detachment rates over time, it can be inferred that over longer durations, the surfactant solution may exhibit stronger oil film detachment potential. The observed phenomena are primarily attributed to the ability of the surfactant to reduce oil–water interfacial tension and improve solid surface wettability, thereby lowering the adhesion work of the oil film and accelerating its detachment. However, due to the processes of diffusion, adsorption, and interfacial reorganization that surfactant molecules must undergo, the initial detachment rate is relatively low, resembling that of pure water in the short term and remaining lower than that of the NB suspension. As the immersion time extends, the surfactant adsorption at the interface gradually approaches saturation, interfacial activity continues to strengthen, and the detachment rate steadily increases, suggesting that over longer time scales, its oil film detachment performance may surpass that of NBs. Nevertheless, the high efficiency demonstrated by NBs in the short term, combined with their lower environmental impact and operational costs compared to surfactants, positions them as a promising, efficient, cost-effective, and environmentally friendly enhanced oil recovery technology.

3.3. NB flow behavior in porous media

3.3.1. Pore-scale flow behavior in a single-channel constricted pore throat

A comparative study of the flow field characteristics of water and NB suspension through a single-channel constricted pore throat was conducted using PIV velocimetry. The experimental results are shown in Fig. 13(a, b). While the flow field distributions of both fluids were largely consistent in the upstream and downstream regions of the pore throat, significant differences were observed within the constricted section. As indicated by the velocity profiles in Fig. 13(c), the flow velocity of the NB suspension through the constricted throat was noticeably lower than that of pure water. These observations can be attributed to the following mechanisms. As the NB suspension flows through the constricted throat, the increased velocity leads to a local pressure drop, causing the NBs to expand. Simultaneously, enhanced turbulent effects in the flow field promote collisions and coalescence among NBs, further increasing their size. These enlarged bubbles adsorb

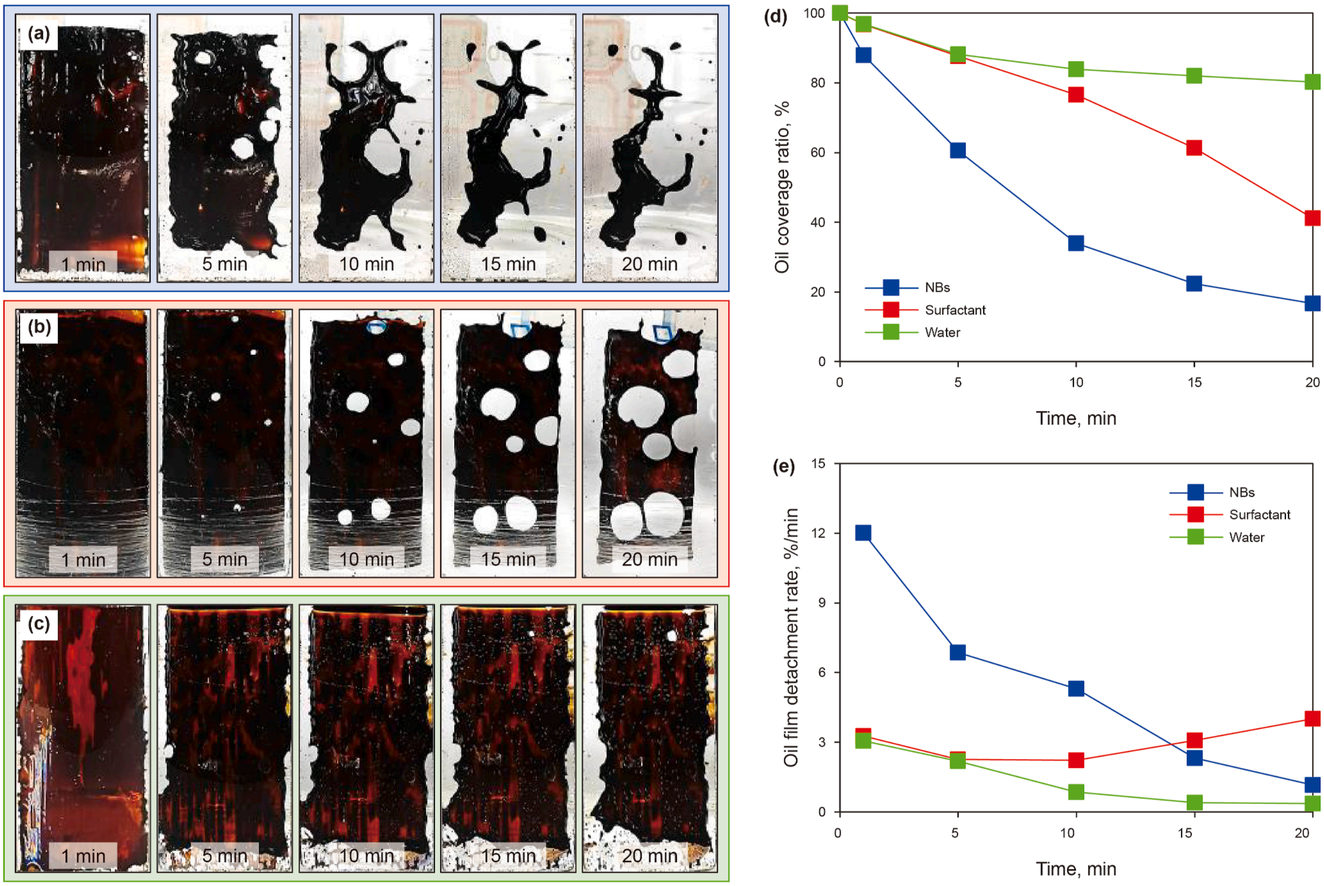

Fig. 11. Experimental results of oil film detachment. Immersion of the oil film in NB suspension (**a**), surfactant (**b**), and water (**c**); changes in the oil coverage ratio (**d**) and detachment rate (**e**) of the oil film at different times in different immersion reagents.

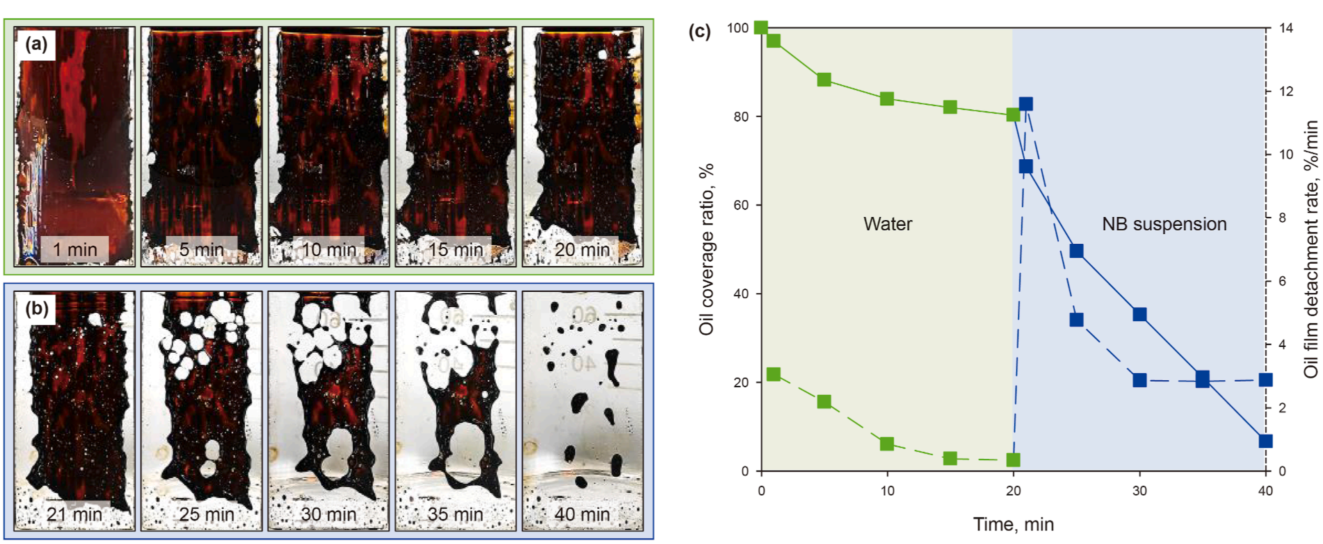

Fig. 12. Images of the oil film change process during its transfer from water (**a**) to NB suspension (**b**). (**c**) Variations of the oil coverage ratio and the oil film detachment rate during the immersion process.

and accumulate along the walls of the constricted section, increasing flow resistance and thereby reducing the velocity through the throat. This demonstrates that NBs can effectively modulate flow resistance and alter the flow field structure as they migrate through constricted pore spaces.

3.3.2. Core-scale flow behavior

Flow experiments in porous media were conducted using two cores with different permeabilities. The variation in pressure differential across the cores as a function of injected volume is shown in Fig. 14. The results indicate that during the pure water injection,

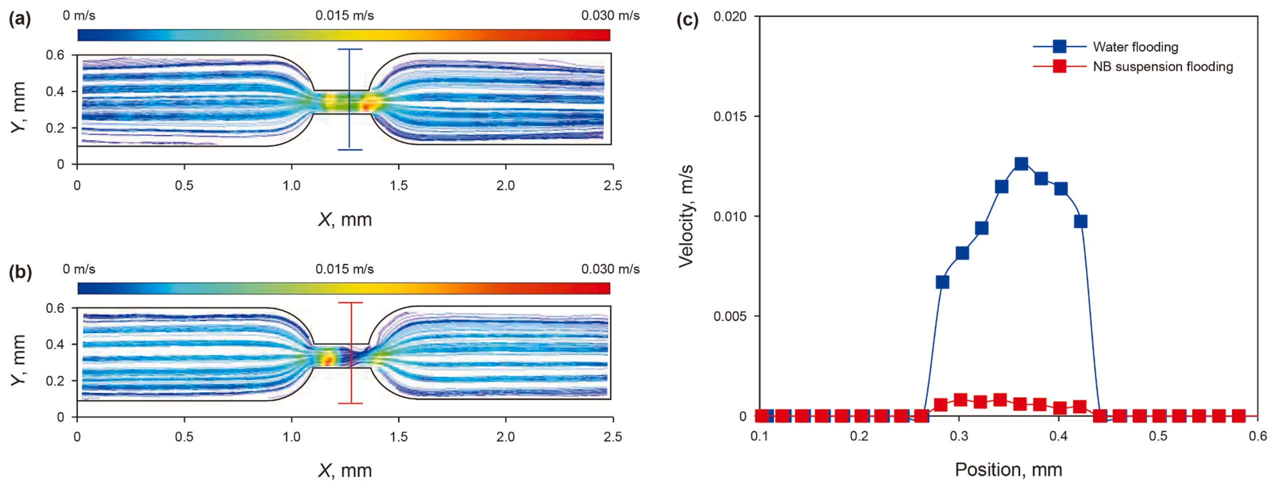

Fig. 13. PIV velocity measurement. Flow fields when water (**a**) and NB suspension (**b**) were injected into the channel, respectively. (**c**) Flow velocity profile at the cross-section.

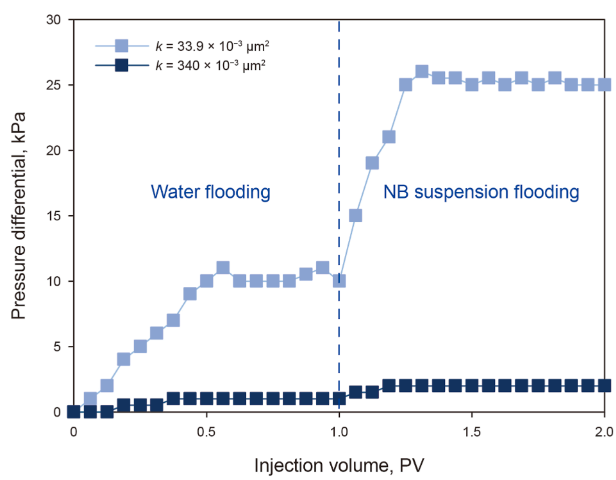

Fig. 14. The curve of pressure differential versus injection volume during water/NB suspension injection.

the pressure differential exhibited an initial slow increase followed by gradual stabilization. When the injected volume reached 1 PV and the fluid was switched to an NB suspension, the pressure differential across the cores showed a secondary increase and eventually stabilized at a new equilibrium state. The stabilized pressure differential during NB injection was 2.0–2.5 times higher than that during water injection, with the low-permeability core exhibiting a greater increase in pressure differential compared to the high-permeability core. These phenomena can be attributed to interactions between NBs and the pore-throat structures of the porous media. First, as previously mentioned, NBs undergo expansion, collision, and aggregation when passing through pore throats, and they adsorb onto the inner surfaces of pore throats in the core. This behavior collectively reduces the effective flow cross-sectional area. Second, the narrow pore-throat structures within the core mechanically trap NBs, inducing a Jamin effect. When NBs pass through constricted channels, they deform and overcome additional capillary resistance, significantly increasing flow resistance. Due to their smaller pore-throat sizes, low-permeability cores exhibit higher mechanical trapping efficiency for NBs, resulting in a more pronounced increase in pressure differential compared to high-permeability cores. These findings fully demonstrate the ability of NBs to modulate flow behavior in porous media, with their effects showing a clear correlation with core permeability.

3.3.3. Two-phase relative permeability curve measurement

Through the measurement of oil–water/NB suspension two-phase relative permeability curves (Fig. 15), the influence of NBs on two-phase relative permeability was investigated. The experimental results demonstrate that the introduction of NBs significantly enhanced the relative permeability of the oil phase while suppressing the relative permeability of the water phase under high water saturation conditions (>50%). This shift caused the oil–water equal-permeability point to move toward higher water saturation by 5.78%, effectively expanding the co-permeability zone. Additionally, the residual oil saturation was reduced from 31.57% to 25.83%, with a decrease of 5.74%. As noted earlier, NBs reduce oil–water interfacial tension and enhance the oleophobicity of solid surfaces, thereby lowering the adhesion work. This promotes the coalescence of oil-film residual oil into mobile droplets, altering the occurrence state of residual oil and improving the mobility of crude oil. Additionally, NBs increase flow resistance in high-permeability channels, diverting subsequent fluids into low-permeability regions. They also enhance the affinity between the displacing fluid and oil-bearing pore walls, enabling access to microporous oil-containing spaces that are

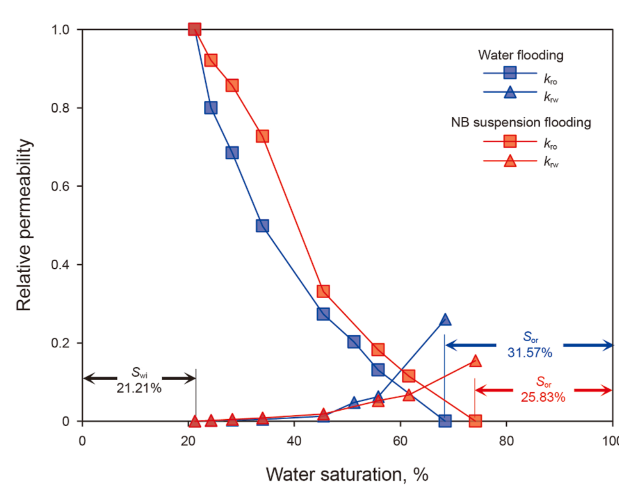

Fig. 15. The curve of oil–water/NB suspension two-phase relative permeability.

unreachable by pure water flooding. The synergy of these two mechanisms effectively expands the sweep efficiency of the displacing fluid, increases the overall oil displacement efficiency in the core, and reduces residual oil saturation.

These phenomena primarily originate from the ability of NBs to modulate flow behavior in porous media and the interfacial properties of the water–oil–solid multiphase system. As previously discussed, NBs reduce oil–water interfacial tension and enhance the oleophobicity of solid surfaces, thereby decreasing adhesion work and promoting the coalescence of oil-film residual oil into mobile droplets. This alters the occurrence state of residual oil and enhances the mobility of crude oil. Additionally, NBs increase flow resistance in high-permeability channels, diverting subsequent fluids into low-permeability regions. They also enhance the affinity between the displacing fluid and the walls of oil-bearing pores, enabling access to microporous oil-containing spaces that are unreachable by pure water flooding. The synergy of these two mechanisms effectively expands the sweep efficiency of the displacing fluid, increases overall oil displacement efficiency in the core, and reduces residual oil saturation.

3.4. NB oil displacement mechanism

3.4.1. Microscopic oil displacement experiment

Microscopic oil displacement experiments were conducted to compare the differences in displacement efficiency between water flooding and NB flooding, with results shown in Fig. 16. At the end of water flooding, significant variations in sweep efficiency were observed across regions with different coordination numbers. Regions with a coordination number of 3 exhibited the highest sweep efficiency (72.18%) but contained numerous isolated, unswept pores. Regions with coordination numbers of 4 and 6 showed lower sweep efficiencies (49.92% and 47.48%, respectively), with pronounced channeling effects but fewer isolated, unswept pores. The overall sweep efficiency of water flooding was 54.19%. In contrast, NB flooding significantly improved displacement performance. The sweep efficiency in regions with a coordination number of 6 increased to 64.3% (a 21.38% improvement), while regions with a coordination number of 4 showed the greatest enhancement, achieving 92.32% (a 44.84% increase). Regions with a coordination number of 3 reached 89.12% (a 16.92% improvement), representing the smallest gain. The overall sweep efficiency of NB flooding was 81.91%, reflecting a 27.72% increase compared to water flooding.

Pore coordination number exerts a critical influence on displacement efficiency. In low-coordination-number regions, limited pore connectivity constricts fluid flow paths, resulting in bypassing and the formation of isolated unswept pores where crude oil remains trapped. In high-coordination-number regions, improved connectivity reduces pore isolation but promotes preferential flow through high-permeability channels, leading to early breakthrough and reduced overall sweep efficiency. NBs significantly enhance displacement performance through two synergistic mechanisms: by increasing flow resistance to expand the sweep range, and by improving the wettability of pore walls to strengthen the affinity between the displacing fluid and oil-bearing pores, thereby significantly enhancing imbibition capability. Notably, the improvement effects of NBs vary across regions with different coordination numbers. In regions with a coordination number of 3, although bubble blocking may further reduce pore connectivity, enhanced imbibition of the displacing fluid in oil-containing pores still achieves certain improvements in sweep efficiency. In regions with a coordination number of 6, moderate improvement is achieved through limited blocking that partially reduces connectivity, combined with enhanced imbibition. Regions with a coordination number of 4 most effectively demonstrate the dual advantages of NBs, as they not only improve connectivity through effective blocking but also fully leverage strong affinity to synergistically expand sweep efficiency, resulting in the most pronounced improvement. These differential improvements stem from the interaction between the limited ability of NBs to modify flow behavior in porous media and the pore structures of regions with varying coordination numbers.

3.4.2. Core flooding experiment

The production enhancement effect of NBs and their mechanisms for improving oil recovery were revealed through displacement experiments conducted in triplicate on cores with

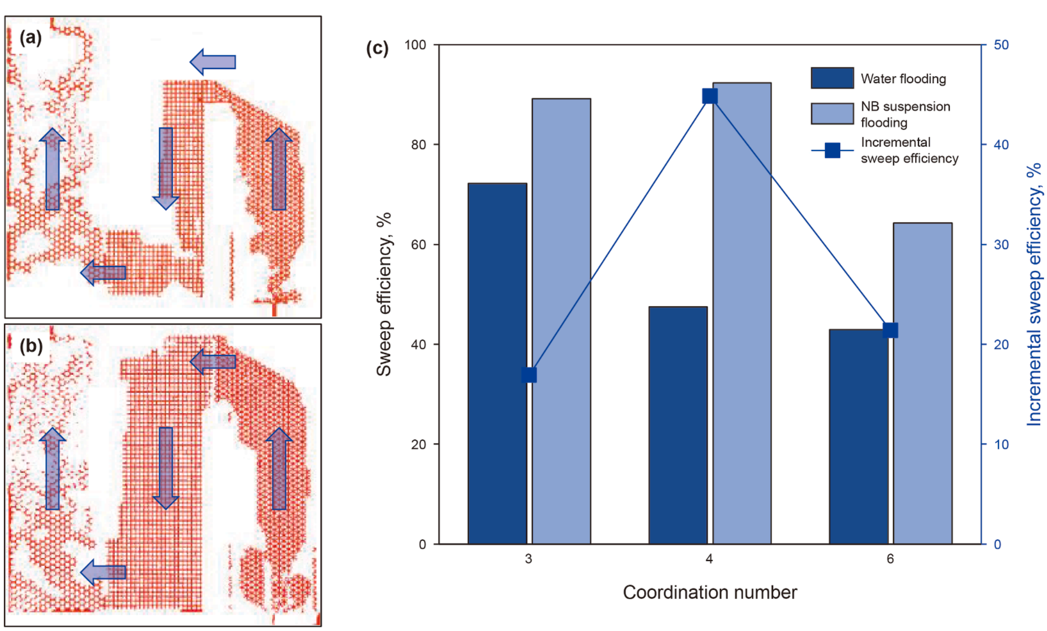

Fig. 16. Results of microscopic oil displacement experiment. Microscopic image at the end of water flooding (**a**) and NB flooding (**b**). (**c**) Comparison of sweep efficiency of water/NB flooding at different coordination numbers.

different permeabilities. Representative curves showing the relationship between oil recovery factor (or water cut) and injection volume from a typical test run are presented in Fig. 17. During water flooding, the following characteristics were observed: As the injection volume increased, the water cut continued to rise, while the pressure differential across the core initially peaked and then gradually declined before stabilizing. A water cut of 98% is reached in the low-permeability core earlier than that in the high-permeability core. The final water flooding recovery rate for the low-permeability core was 29.29%, which was 9.84% lower than that of the high-permeability core (39.13%). After switching to NB flooding, the water cut in both the high- and low-permeability cores decreased by approximately 18%, and the pressure differential increased significantly, stabilizing at 2.0–2.5 times the level observed during the stable phase of water flooding. In terms of recovery efficiency, NB flooding improved the recovery rate of the high-permeability core by 6.42%, achieving a final recovery rate of 45.55%. The low-permeability core exhibited a more pronounced enhancement, with a recovery rate increase of 9.14% and a final recovery rate of 38.43%. These results demonstrate that NBs have a significant production enhancement effect. The results of triplicate parallel experiments demonstrated that in the presence of NBs, the oil recovery from the 340×10^{-3} μm^2 core was increased by 9.14%, 9.44%, and 8.75%, with a mean of 9.11%, while the oil recovery from the 33.9×10^{-3} μm^2 core was increased by 6.42%, 6.80%, and 6.28%, with a mean of 6.49%. These findings verify that the enhancement of oil recovery attributed to that NBs possess sound stability and reliability.

The mechanism by which NBs enhance oil recovery primarily involves their ability to modulate flow behavior in porous media and interfacial properties. NBs adsorb and coalesce within pores to form larger bubbles, significantly increasing flow resistance. Simultaneously, they facilitate the coalescence of oil-film residual oil remaining on pore walls after water flooding into mobile droplets and promote their detachment from the pore surfaces. These detached droplets further generate a Jamin effect during migration, synergistically enhancing flow resistance, effectively suppressing channeling of the displacing fluid, and expanding its sweep range. As previously mentioned, NBs also alter the wettability of pore walls, which not only reduces crude oil retention during flow but also enhances the affinity between the displacing fluid and oil-bearing pore surfaces. This strengthens spontaneous imbibition, enabling the displacing fluid to penetrate microporous oil-trapped regions inaccessible to pure water. In low-permeability cores, the smaller pore sizes cause NBs to be more easily retained, thereby enhancing their effect on increasing flow resistance. This enables more effective blocking of dominant flow channels and redirects subsequent fluids toward unswept regions, ultimately expanding the sweep range. Moreover, compared to high-permeability cores, low-permeability cores contain a higher proportion of microporous oil-bearing spaces that are challenging for water to access. These combined mechanisms allow NBs to demonstrate more pronounced production enhancement effects in low-permeability reservoirs.

This study employed artificial cores for the core flooding experiments, primarily due to their advantages of relatively

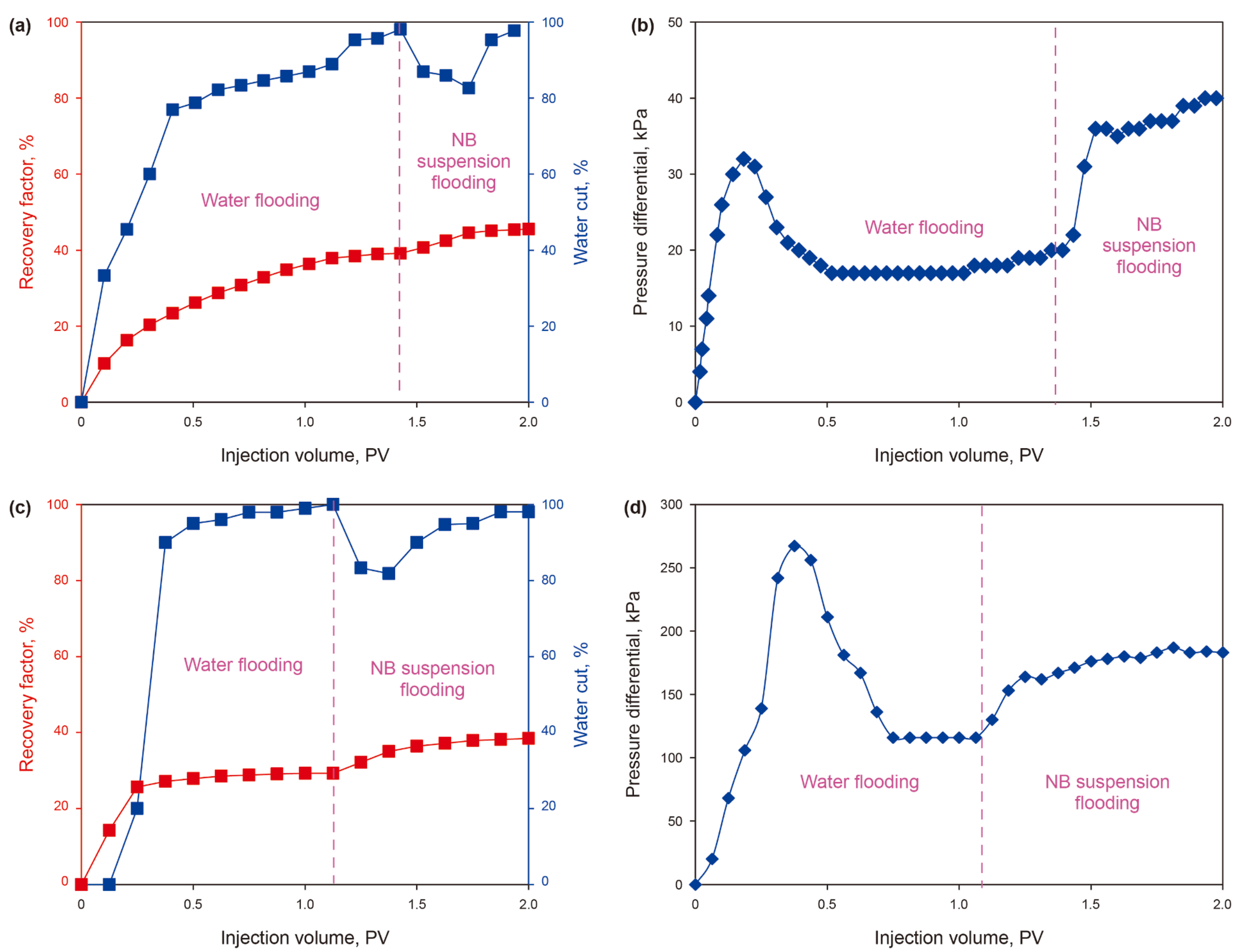

Fig. 17. The curves of recovery factor, water cut, pressure differential versus injection volume in cores with different permeabilities. (**a**, **b**) 340×10^{-3} μm^2; (**c**, **d**) 33.9×10^{-3} μm^2.

controllable pore structure and high reproducibility, which facilitate research at the mechanistic level. Compared with natural cores, artificial cores have a more homogeneous pore structure and relatively simple mineral composition (Han et al., 2016), which may reduce the adsorption and retention of NBs in the pores, weaken their interactions with crude oil and the pore matrix, and consequently lead to an observed enhancement in oil recovery that underestimates their potential in real reservoirs. Therefore, this study focuses more on elucidating the mechanisms of NBs in EOR. Subsequent research will utilize natural cores to further evaluate the enhanced oil recovery performance of NBs under complex real reservoir conditions.

4. Conclusions

This study investigated the influence of environmental factors, including salinity degree, temperature, external shear, and time, on the size and concentration of nanobubbles (NBs). The interfacial properties of NBs were analyzed through oil–water interfacial tension and contact angle measurements, combined with oil film detachment experiments. Based on pore-scale and core-scale flow and oil displacement experiments, the flow characteristics of NBs in porous media and their mechanisms for enhancing oil recovery were revealed. The main conclusions are as follows:

(1) NBs exhibit excellent stability under varying environmental conditions (including salinity, temperature, shear duration, and shear rate), with their average size consistently maintained within the range of 175–300 nm and their concentration stable at the order of 10^7 particles/mL.
(2) NBs reduce oil–water interfacial tension by 1.66–2.95 mN/m while increasing the underwater contact angle of crude oil by 16°, thereby enhancing the affinity of solid surfaces to the aqueous phase and strengthening their oil-repellent properties. These interfacial modifications enhance spontaneous imbibition, enabling NBs to access microporous regions inaccessible to conventional water flooding and expanding the sweep range of the displacing fluid.
(3) NBs significantly accelerate and enhance oil film detachment, thereby markedly improving oil-washing efficiency. Under identical immersion durations, the peak oil film detachment rate in NB suspension (11.59 %/min) was four times higher than that in pure water (2.9 %/min). After 20 min of immersion, NBs reduced the oil-covered area by 83.38%, compared to only 19.7% in water—a 4.23-fold improvement. When an oil film pre-immersed in water for 20 min was transferred to an NB suspension, the detachment rate increased by 33 times, and the oil-covered area ratio rapidly decreased from 80.3% to 6.73%, demonstrating the exceptional oil-washing capability of NBs. Furthermore, the oil film detachment effect of NBs within a short period (20 min) is superior to that of the surfactant solution (0.1 wt% sodium dodecyl benzene sulfonate).
(4) NBs alter local flow dynamics near constricted pore throats through expansion, coalescence, and adsorption, increasing aqueous phase flow resistance by a factor of 2.0–2.5. They significantly enhance oil relative permeability while suppressing water relative permeability at high water saturation (>50%), expanding the oil–water co-flow zone and reducing residual oil saturation by 5.74%.
(5) NBs effectively suppress channeling of the displacing fluid and expand its sweep range by 27.72% compared to water flooding. The extent of sweep improvement varies with pore coordination numbers, with the most pronounced enhancement (44.84%) observed in regions with a coordination number of 4. NB flooding increased oil recovery in high-permeability and low-permeability cores by 6.49% and 9.11%, respectively, indicating more significant production enhancement in low-permeability reservoirs.

CRediT authorship contribution statement

Xu-Wen Qin: Writing – original draft, Methodology, Investigation, Formal analysis, Data curation, Conceptualization. **Bei Wei:** Visualization, Validation, Investigation. **Yong-Sheng Liu:** Resources, Formal analysis, Data curation. **Qian Chen:** Validation, Methodology, Investigation. **Hao-Yu Zheng:** Visualization, Data curation. **Er-Meng Zhao:** Supervision, Resources. **Qing-Jun Du:** Supervision, Resources, Project administration. **Kang Zhou:** Supervision, Formal analysis. **Yong-Ge Liu:** Software, Resources. **Wei-Bing Tian:** Supervision, Resources. **Jian Hou:** Writing – review & editing, Supervision, Resources, Project administration, Funding acquisition.

Declaration of competing interest

The authors declare that they have no known competing financial interests or personal relationships that could have appeared to influence the work reported in this paper.

Acknowledgments

The authors greatly appreciate the financial support of Important National Science and Technology Specific Projects of China (No. 2025ZD1404403), Fund of State Key Laboratory of Deep Oil and Gas, China University of Petroleum (East China) (No. SKLDOG2024-ZYRC-04), Science and Technology Support Plan for Youth Innovation of Colleges and Universities of Shandong Province (No. 2024KJH122), and Taishan Scholars Program of Shandong Province.

References

Aarra, M.G., Skauge, A., Solbakken, J., 2014. Properties of N_2- and CO_2-foams as a function of pressure. J. Pet. Sci. Eng. 116, 72–80. https://doi.org/10.1016/j.petrol.2014.02.017.
Abdulsada, J.A., Chen, H., Wei, B., et al., 2025. A mini-review of water-alternating-CO_2 injection process and derivations for enhanced oil recovery and CO_2 storage in subsurface reservoirs. Petroleum 11 (4), 410–421. https://doi.org/10.1016/j.petlm.2025.07.001.
Agarwal, K., Trivedi, M., Nirmalkar, N., 2022. Does salting-out effect nucleate nanobubbles in water: Spontaneous nucleation? Ultrason. Sonochem. 82, 105860. https://doi.org/10.1016/j.ultsonch.2021.105860.
Agarwal, K., Dutta, N., Nirmalkar, N., 2023. Mechanistic insights into surface tension reduction: The potential contribution of nanobubbles. J. Mol. Liq. 647, 264–276. https://doi.org/10.1016/j.jcis.2023.05.082.
Ajoma, E., Saira, Sungkachart, T., et al., 2020. Water-saturated CO_2 injection to improve oil recovery and CO_2 storage. Appl. Energy 266, 114853. https://doi.org/10.1016/j.apenergy.2020.114853.
Bai, M., Zhang, Z., Fu, X., 2016. A review on well integrity issues for CO_2 geological storage and enhanced gas recovery. Renew. Sustain. Energy Rev. 59, 920–926. https://doi.org/10.1016/j.rser.2016.01.043.
Bai, M., Jia, Y., Liu, Z., et al., 2025. Degradation mechanism of organic contaminants in complex contaminated groundwater in landfill sites with oxygen micro-nano-bubbles aeration. J. Water Process Eng. 69, 106635. https://doi.org/10.1016/j.jwpe.2024.106635.
Chen, B., Reynolds, A.C., 2018. CO_2 water-alternating-gas injection for enhanced oil recovery: Optimal well controls and half-cycle lengths. Comput. Chem. Eng. 113, 44–56. https://doi.org/10.1016/j.compchemeng.2018.03.006.
Chen, M., Cheng, L., Wang, X., et al., 2019. Pore network modelling of fluid flow in tight formations considering boundary layer effect and media deformation. J. Pet. Sci. Eng. 180, 643–659. https://doi.org/10.1016/j.petrol.2019.05.072.
Chen, X., Zhang, Q., Trivedi, J., et al., 2024. Investigation on enhanced oil recovery and CO_2 storage efficiency of temperature-resistant CO_2 foam flooding. Fuel 364, 130870. https://doi.org/10.1016/j.fuel.2024.130870.

Dien, L.T., Linh, N.V., Mai, T.T., et al., 2022. Impacts of oxygen and ozone nanobubbles on bacteriophage in aquaculture system. Aquaculture 551, 737894. https://doi.org/10.1016/j.aquaculture.2022.737894.

Elnaggar, H., Taman, A., Ali, R., et al., 2025. Oil recovery enhancement by N_2 nanobubbles. Energy Fuels 39 (5), 2482–2499. https://doi.org/10.1021/acs.energyfuels.4c05180.

Guo, M., Song, B., Chen, R., et al., 2025. Enhanced atrazine degradation in contaminated groundwater using ozone micro-nanobubbles: Reactivity, kinetics and mechanisms. Colloids Surf., A Physicochem. Eng. Asp. 726 (2), 137811. https://doi.org/10.1016/j.colsurfa.2025.137811.

Han, D., Lu, X., Wang, T., et al., 2016. Difference of pore structure between artificial cores and natural cores and its influence on the seepage characteristics of oil displacement agent. Pet. Geol. Recovery Effic. 23 (4), 82–87. https://doi.org/10.13673/j.cnki.cn37-1359/te.2016.04.013 (in Chinese).

Ho, W., Lin, W., Verpoort, F., et al., 2023. Application of novel nanobubble-contained electrolyzed catalytic water to cleanup petroleum-hydrocarbon contaminated soils and groundwater: A pilot-scale and performance evaluation study. J. Environ. Manag. 347, 119058. https://doi.org/10.1016/j.jenvman.2023.119058.

Hu, L., Xia, Z., 2018. Application of ozone micro-nano-bubbles to groundwater remediation. J. Hazard. Mater. 342, 446–453. https://doi.org/10.1016/j.jhazmat.2017.08.030.

Jia, H., Yu, H., Wang, S., et al., 2024. Investigation of CO_2 microbubble assisted carbon sequestration and gravity-induced microbubble ripening in low permeability reservoirs. Appl. Energy 373, 123954. https://doi.org/10.1016/j.apenergy.2024.123954.

Jia, H.W., Yu, H.Y., Ma, R., 2025. Experimental study of EOR mechanisms of non-chemical CO_2 microbubbles and their impact on pore structures. Pet. Sci. 22 (3), 1214–1224. https://doi.org/10.1016/j.petsci.2025.01.001.

Jia, J., Cai, H., Liang, Y., et al., 2023. Synergistic effect of hydrolyzed polyacrylamide and ionic surfactant to enhance the stability of CO_2 foam: A molecular dynamics study. Pet. Sci. Bull. 8 (1), 69–86. https://doi.org/10.3969/j.issn.2096-1693.2023.01.005 (in Chinese).

Jiang, L., Xue, Z., Park, H., 2019. Enhancement of CO_2 dissolution and sweep efficiency in saline aquifer by micro bubble CO_2 injection. Int. J. Heat Mass Tran. 138, 1211–1221. https://doi.org/10.1016/j.ijheatmasstransfer.2019.04.139.

Jin, N., Zhang, F., Cui, Y., et al., 2022. Environment-friendly surface cleaning using micro-nano bubbles. Particuology 66, 1–9. https://doi.org/10.1016/j.partic.2021.07.008.

Ke, S., Xiao, W., Quan, N., et al., 2019. Formation and stability of bulk nanobubbles in different solutions. Langmuir 35 (15), 5250–5256. https://doi.org/10.1021/acs.langmuir.9b00144.

Kim, D., Han, J., 2020. Remediation of copper contaminated soils using water containing hydrogen nanobubbles. Appl. Sci. 10 (6), 2185. https://doi.org/10.3390/app10062185.

Lei, J., Huang, D., Zhao, W., et al., 2024. Investigating the stability mechanisms of single bulk nanobubbles: A molecular dynamics perspective. Int. J. Heat Mass Tran. 225, 125407. https://doi.org/10.1016/j.ijheatmasstransfer.2024.125407.

Li, H., Hu, L., Song, D., et al., 2014. Subsurface transport behavior of micro-nano bubbles and potential applications for groundwater remediation. Int. J. Environ. Res. Publ. Health 11 (1), 473–486. https://doi.org/10.3390/ijerph110100473.

Li, K., Zhou, J., Matkarimov, S.T., et al., 2025. Insights into the roles of interfacial micro/nano bubbles on mineral surfaces and their implications on fine chalcopyrite flotation. Surf. Interfaces 60, 106063. https://doi.org/10.1016/j.surfin.2025.106063.

Li, X., Peng, B., Liu, Q., et al., 2023. Micro and nanobubbles technologies as a new horizon for CO_2-EOR and CO_2 geological storage techniques: A review. Fuel 341, 127661. https://doi.org/10.1016/j.fuel.2023.127661.

Lin, Y., Pu, B., Cheng, L., et al., 2024. A modified probability-based pore network model considering particle plugging for characterizing velocity-sensitive damage. Energy Fuels 38 (17), 16782–16794. https://doi.org/10.1021/acs.energyfuels.4c02747.

Liu, S., Oshita, S., Makino, Y., et al., 2016. Oxidative capacity of nanobubbles and its effect on seed germination. ACS Sustain. Chem. Eng. 4 (3), 1347–1353. https://doi.org/10.1021/acssuschemeng.5b01368.

Lu, J., Huang, X., Zhang, Z., et al., 2022. Co-coagulation of micro-nano bubbles (MNBS) for enhanced drinking water treatment: A study on the efficiency and mechanism of a novel cleaning process. Water Res. 226, 119245. https://doi.org/10.1016/j.watres.2022.119245.

Lu, Z., Xie, J., Zhu, D., et al., 2024. The combination of nanobubble aeration and iron-based multi-carbon source composites achieves efficient aquaculture wastewater nitrogen removal. Chem. Eng. J. 491, 152093. https://doi.org/10.1016/j.cej.2024.152093.

Ma, F., Zhang, P., Tao, D., 2022. Surface nanobubble characterization and its enhancement mechanisms for fine-particle flotation: A review. Int. J. Min. Met. Mater. 29, 727–738. https://doi.org/10.1007/s12613-022-2450-3.

Ma, X., Li, M., Sun, C., 2024. Effect of ionic environment in aqueous solution on nucleation and stabilization of bulk nanobubbles. Appl. Surf. Sci. 656, 159726. https://doi.org/10.1016/j.apsusc.2024.159726.

Marcelino, K.R., Ling, L., Wongkiew, S., et al., 2023. Nanobubble technology applications in environmental and agricultural systems: Opportunities and challenges. Crit. Rev. Environ. Sci. Technol. 53, 1378–1403. https://doi.org/10.1080/10643389.2022.2136931.

Oh, S.H., Kim, J.M., 2017. Generation and stability of bulk nanobubbles. Langmuir 33 (15), 3818–3823. https://doi.org/10.1021/acs.langmuir.7b00510.

Pal, P., Anantharaman, H., 2022. CO_2 nanobubbles utility for enhanced plant growth and productivity: Recent advances in agriculture. J. CO_2 Util. 61. https://doi.org/10.1016/j.jcou.2022.102008.

Rafryanto, A.F., Ramadina, Z.D.P., Nur'aini, S., et al., 2024. High recovery of ceramic membrane cleaning remediation by ozone nanobubble technology. ACS Omega 9 (10), 11484–11493. https://doi.org/10.1021/acsomega.3c08379.

Rognmo, A.U., Heldal, S., Ferno, M.A., 2018. Silica nanoparticles to stabilize CO_2-foam for improved CO_2 utilization: Enhanced CO_2 storage and oil recovery from mature oil reservoirs. Fuel 216, 621–626. https://doi.org/10.1016/j.fuel.2017.11.144.

Sarlak, M., Farbod, A., Tabatabaei Nezhad, S.A., et al., 2021. Experimental investigation of CO_2 in continuous and water alternating gas injection. Pet. Sci. Technol. 39 (6), 165–174. https://doi.org/10.1080/10916466.2010.549894.

Shukla, R., Ranjith, P., Haque, A., et al., 2010. A review of studies on CO_2 sequestration and caprock integrity. Fuel 89 (10), 2651–2664. https://doi.org/10.1016/j.fuel.2010.05.012.

Taman, A., Shoukry, A.E., Kubelka, J., et al., 2025. Oil recovery enhancement by nanobubbles: Insights from high-pressure micromodel studies. J. Colloid Interface Sci. 693, 137647. https://doi.org/10.1016/j.jcis.2025.137647.

Temesgen, T., Bui, T.T., Han, M., et al., 2017. Micro and nanobubble technologies as a new horizon for water-treatment techniques: A review. Adv. Colloid Interface Sci. 246, 40–51. https://doi.org/10.1016/j.cis.2017.06.011.

Tripathi, R., Alcorn, Z.P., Graue, A., et al., 2024. Combination of non-ionic and cationic surfactants in generating stable CO_2 foam for enhanced oil recovery and carbon storage. Adv. Geo-Energy Res. 13 (1), 42–55. https://doi.org/10.46690/ager.2024.07.06.

Tuziuti, T., Yasui, K., Kanematsu, W., 2023. Decrease in the surface tension of nanobubble dispersion in water: Results of surface excess of bulk nanobubbles at interfaces. Langmuir 39 (16), 5771–5778. https://doi.org/10.1021/acs.langmuir.3c00040.

Ushikubo, F.Y., Furukawa, T., Nakagawa, R., et al., 2010. Evidence of the existence and the stability of nano-bubbles in water. Colloids Surf., A Physicochem. Eng. Asp. 361 (1-3), 31–37. https://doi.org/10.1016/j.colsurfa.2010.03.005.

Wang, S., Wang, Z., Lv, P., et al., 2025. CO_2 micro-nanobubble technology in carbon capture, utilization, and storage: A mini review. Energy Fuels 39 (5), 2381–2395. https://doi.org/10.1021/acs.energyfuels.4c05183.

Wang, Y., Wang, T., 2023. Preparation method and application of nanobubbles: A review. Coatings 13 (9), 1510. https://doi.org/10.3390/coatings13091510.

Wang, Z., An, C., Lee, K., et al., 2023. Exploring the role of nanobubbles in the fate and transport of spilled oil on shorelines. ACS ES&T Water 3 (1), 30–40. https://doi.org/10.1021/acsestwater.2c00344.

Wu, J., Zhang, K., Cen, C., et al., 2021. Role of bulk nanobubbles in removing organic pollutants in wastewater treatment. AMB Express 11, 96. https://doi.org/10.1186/s13568-021-01254-0.

Xiao, Y., Liu, H., Sun, C., et al., 2025. Research progress of micro-nano bubbles in environmental remediation: Mechanisms, preparation methods, and applications. J. Environ. Manag. 375, 124387. https://doi.org/10.1016/j.jenvman.2025.124387.

Yang, D., Zhao, Z., Gong, L., et al., 2023. Surface interaction mechanisms of air bubbles, asphaltenes and oil drops in aqueous solutions with implications for interfacial engineering processes. J. Colloid Interface Sci. 647, 264–276. https://doi.org/10.1016/j.jcis.2023.05.082.

Yang, Z., Wang, Y., Lukwambe, B., et al., 2024. Using ozone nanobubbles, and microalgae to promote the removal of nutrients from aquaculture wastewater: Insights from the changes of microbiomes. Environ. Res. 257, 19349. https://doi.org/10.1016/j.envres.2024.119349.

Zhang, C., Zhang, Q., Wang, W., et al., 2022. Capillary and viscous forces during CO_2 flooding in tight reservoirs. Capillarity 5 (6), 105–114. https://doi.org/10.46690/capi.2022.06.01.

Zhang, F., Cai, H., Fan, G., et al., 2024a. The role of interfacial nanobubbles in the flotation performance of microfine particles. Colloids Surf., A Physicochem. Eng. Asp. 699, 134633. https://doi.org/10.1016/j.colsurfa.2024.134633.

Zhang, L., Wang, Y., Chen, X., et al., 2025. Elucidating the multiscale synergistic enhancement of oil film mobilization-stripping by microbubble coalescence. Ind. Eng. Chem. Res. 64 (33), 16323–16340. https://doi.org/10.1021/acs.iecr.5c01692.

Zhang, Y., Wang, Y., Xue, F., et al., 2015. CO_2 foam flooding for improved oil recovery: Reservoir simulation models and influencing factors. J. Pet. Sci. Eng. 133, 838–850. https://doi.org/10.1016/j.petrol.2015.04.003.

Zhang, Y., Cai, L., Chen, L., et al., 2024b. Effect of micro-nano bubbles on the remediation of saline-alkali soil with microbial agent. Sci. Total Environ. 912, 168940. https://doi.org/10.1016/j.scitotenv.2023.168940.

Zhao, F., Wang, P., Huang, S., et al., 2020. Performance and applicable limits of multi-stage gas channeling control system for CO_2 flooding in ultra-low permeability reservoirs. J. Pet. Sci. Eng. 192, 107336. https://doi.org/10.1016/j.petrol.2020.107336.

Zhu, D., Lu, J., Zhang, J., et al., 2025. N_2 and CO_2 nanobubble enhanced oil recovery in conglomerate reservoirs based on NMR technology. Energy Fuels 39 (28), 13378–13385. https://doi.org/10.1021/acs.energyfuels.5c02717.

Zinjenab, Z.T., Azimi, E., Shadman, M., et al., 2023. Nano-microbubbles and feed size interaction in lead and zinc sulfide minerals flotation. Chem. Eng. Process. Process Intensif. 189, 109401. https://doi.org/10.1016/j.cep.2023.109401.